

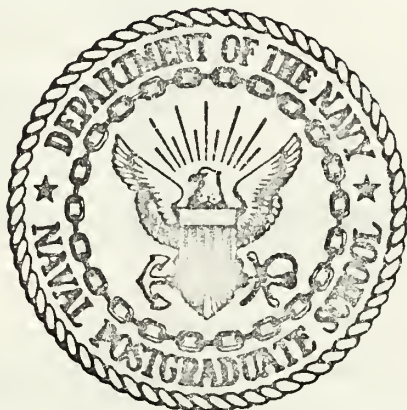
A PROPOSED METHOD TO MEASURE DIELECTRIC
PROPERTIES OF NON-SPHERICAL PARTICLES
USING A FABRY-PEROT INTERFEROMETER
AND MULTIPASS REFLECTIVE CELL

Anthony Raniszewski

DUDLEY KNOX LIBRARY
NAVAL POSTGRADUATE SCHOOL
MONTEREY, CALIFORNIA 93940

NAVAL POSTGRADUATE SCHOOL

Monterey, California



THESIS

A PROPOSED METHOD TO MEASURE DIELECTRIC
PROPERTIES OF NON-SPHERICAL PARTICLES
USING A FABRY-PEROT INTERFEROMETER
AND MULTIPASS REFLECTIVE CELL

by

Anthony Raniszewski

June 1975

Thesis Advisor:

W.M. Tolles

Approved for public release; distribution unlimited.

T168209

REPORT DOCUMENTATION PAGE		READ INSTRUCTIONS BEFORE COMPLETING FORM
1. REPORT NUMBER	2. GOVT ACCESSION NO.	3. RECIPIENT'S CATALOG NUMBER
4. TITLE (and Subtitle) A Proposed Method to Measure Dielectric Properties of Non-Spherical Particles Using a Fabry-Perot Interferometer and Multipass Reflective Cell		5. TYPE OF REPORT & PERIOD COVERED Master's Thesis; June 1975
7. AUTHOR(s) Anthony Raniszewski		6. PERFORMING ORG. REPORT NUMBER
9. PERFORMING ORGANIZATION NAME AND ADDRESS Naval Postgraduate School Monterey, California 93940		8. CONTRACT OR GRANT NUMBER(s)
11. CONTROLLING OFFICE NAME AND ADDRESS Naval Postgraduate School Monterey, California 93940		10. PROGRAM ELEMENT, PROJECT, TASK AREA & WORK UNIT NUMBERS
14. MONITORING AGENCY NAME & ADDRESS (if different from Controlling Office)		12. REPORT DATE June 1975
		13. NUMBER OF PAGES 101
		15. SECURITY CLASS. (of this report) Unclassified
		15a. DECLASSIFICATION/DOWNGRADING SCHEDULE
16. DISTRIBUTION STATEMENT (of this Report) Approved for public release; distribution unlimited.		
17. DISTRIBUTION STATEMENT (of the abstract entered in Block 20, if different from Report)		
18. SUPPLEMENTARY NOTES		
19. KEY WORDS (Continue on reverse side if necessary and identify by block number)		
20. ABSTRACT (Continue on reverse side if necessary and identify by block number) A method was proposed to investigate the dielectric properties of non-spherical particles in suspension. The system employed resonance shifts of a Fabry-Perot interferometer and beam attenuation of a multipass reflective cell. The theory was developed to support this design and experiments were conducted which verified its feasibility. Zinc oxide particles in suspension acted as a cavity		

(20. ABSTRACT Continued)

perturbation and did show frequency shifts and attenuation. The method employed wavelengths of 6328 Å and 10.6μ but can be modified to use a variety of wavelengths and laser power ranges. Although zinc oxide was the only material used the system has the potential to be used with a wide variety of particulate suspensions.

A Proposed Method to Measure Dielectric
Properties of Non-Spherical Particles
Using a Fabry-Perot Interferometer
and Multipass Reflective Cell

by

Anthony Raniszewski
Captain, United States Marine Corps
B.S., Farleigh Dickinson University, 1968

Submitted in partial fulfillment of the
requirements for the degree of

MASTER OF SCIENCE IN PHYSICS

from the

NAVAL POSTGRADUATE SCHOOL
June 1975

$T_{H2} =$
 $P_{H2} =$
 $C_{H2} =$

ABSTRACT

A method was proposed to investigate the dielectric properties of non-spherical particles in suspension. The system employed resonance shifts of a Fabry-Perot interferometer and beam attenuation of a multipass reflective cell.

The theory was developed to support this design and experiments were conducted which verified its feasibility. Zinc oxide particles in suspension acted as a cavity perturbation and did show frequency shifts and attenuation. The method employed wavelengths of 6328\AA and 10.6μ but can be modified to use a variety of wavelengths and laser power ranges. Although zinc oxide was the only material used the system has the potential to be used with a wide variety of particulate suspensions.

TABLE OF CONTENTS

I.	INTRODUCTION -----	10
II.	THEORY -----	13
	A. BASIC SUSCEPTIBILITY THEORY -----	13
	1. Intrinsic Susceptibility -----	13
	2. Susceptibility and Attenuation -----	19
	3. Aerosol Effects -----	21
	B. MULTIPASS REFLECTIVE CELL -----	23
	1. Basic Theory -----	23
	2. Perturbation Effects -----	29
	C. FABRY-PEROT INTERFEROMETER -----	30
	1. Basic Theory -----	30
	2. Mode Matching -----	37
	3. Cavity Perturbations -----	40
	D. SUMMARY -----	44
III.	EXPERIMENTAL -----	45
	A. SAMPLE PREPARATION -----	45
	B. EXPERIMENTAL PROCEDURE -----	48
	1. Multipass Reflective Cell -----	48
	2. Fabry-Perot Interferometer -----	54
	C. CAVITY DESIGNS -----	60
	1. Initial Multipass Cell -----	60
	2. Final Multipass Cell -----	64
	3. Fabry-Perot Interferometer -----	68
	D. SUPPORTING EQUIPMENT -----	73

1.	Micro-Voltmeter -----	73
2.	Oscilloscope -----	74
3.	Piezo-Electric Translating Circuit --	74
4.	Detectors -----	76
a.	Thermopile -----	76
b.	Lead-Tin-Telluride -----	76
5.	Collimator -----	76
6.	Helium-Neon Laser -----	79
7.	CO ₂ Laser -----	79
IV.	RESULTS -----	80
A.	MULTIPASS REFLECTIVE CELL -----	80
1.	Problems Encountered -----	80
2.	Preliminary Zinc Oxide Results -----	82
B.	FABRY-PEROT INTERFEROMETER -----	87
1.	Problems Encountered -----	87
2.	Preliminary Zinc Oxide Results -----	88
V.	SUMMARY AND CONCLUSIONS -----	97
	BIBLIOGRAPHY -----	99
	INITIAL DISTRIBUTION LIST -----	101

LIST OF FIGURES

1.	Particle Effective Field -----	14
2a.	Particle Intrinsic Susceptibility - Sphere --	17
2b.	Particle Intrinsic Susceptibility - Cylinder -----	18
3.	Beam Path Multipass Reflective Cell -----	23
4.	Beam Path Multipass Reflective Cell -----	23
5.	Determination of Minimum Mirror Length for Multipass Reflective Cell -----	26
6.	Basic Interferometer Design -----	32
7.	Beam Radius -----	32
8.	Cavity Finesse -----	36
9.	Beam Waist -----	38
10.	Cavity Perturbation Effects -----	41
11.	Sample Preparation -----	47
12.	Block Diagram - Multipass Reflective Cell ---	49
13.	Multipass Reflective Cell Mirror Reflections -----	51
14.	Block Diagram - Fabry-Perot Interferometer --	55
15.	Initial Multipass Reflective Cell -----	62
16a.	Final Multipass Reflective Cell -----	66
16b.	Final Multipass Reflective Cell - Illustration -----	67
17a.	Fabry-Perot Interferometer -----	69
17b.	Fabry-Perot Interferometer - Illustration ---	70
18.	Piezoelectric Translator -----	75
19.	Laser Collimator -----	78

20.	Unchopped Multipass Reflective Cell Output ---	83
21.	Chopped Multipass Reflective Cell Output - HeNe -----	84
22.	Chopped Multipass Reflective Cell Output - CO ₂ -----	86
23.	Fabry-Perot Finesse -----	89
24.	Fabry-Perot Cavity Stability -----	89
25a.	Fabry-Perot Perturbation Output -----	91
25b.	Fabry-Perot Perturbation Output -----	91
26.	Fabry-Perot Perturbation Output -----	94
27.	Fabry-Perot Perturbation Output -----	94
28.	Fabry-Perot Perturbation Output -----	95

ACKNOWLEDGEMENT

The author would like to acknowledge the invaluable assistance afforded by Professor William Tolles. Without his concerned effort and the extra time spent to help overcome many problems, this study could not have been completed.

A special note of thanks must be given to Mr. Robert Sanders, whose technical knowledge greatly assisted the author.

Thanks must also be given to Professor Gordon Schacher, who in the absence of Professor Tolles, rendered invaluable advice in the drafting of this study.

I. INTRODUCTION

Dielectric properties of condensed phase media may be measured by creating aerosols and measuring the aerosol dielectric properties. The term aerosol is taken to mean a dispersion of microscopic particles in a gas. Hedy and Brock in Ref. 1 describe several methods presently used to investigate the properties of highly dispersed aerosols (H.D.A.). The methods are divided into two main groups, those using aerosols in a suspended state and those based on the examination of deposits. For aerosols in a suspended state the particle properties are frequently determined from light scattering measurements. For extremely small particles, vapors of other substances are evaporated on them to enable optical methods to be used.

A new method was recently introduced to measure the dielectric properties of aerosols at microwave frequencies (Tolles in Ref. 2), using cavity perturbation techniques. In this work a shift and attenuation in the resonance of a microwave cavity was observed when a non-spherical aerosol suspension of zinc oxide was introduced into the cavity. This shift, attenuation, and rotational relaxation properties could then be related to the particle dimensions and intrinsic dielectric properties. The above description suggests a similar method may be employed in the infra-red using optical cavities. These would measure the real and

imaginary parts of the particle susceptibility. These properties may also be measured by scattering techniques, but this is usually applied to spherical particles and then normally only the real part of the susceptibility is obtained.

This study represents a new extension of cavity perturbation techniques for measuring the infra-red properties of suspended particles without resort to magnification or precipitation. The apparatus is relatively compact and insensitive to many laboratory instabilities. It can be applied to a great variety of particulate suspensions with little or no modification. For these reasons this study should be of interest to those engaged in aerosol physics or pollution research.

The primary objective of this study is to develop a method for measuring the susceptibility of non-spherical aerosols. This can be done by means of 1) a resonance change of a Fabry-Perot interferometer and 2) beam intensity attenuation of a multipass reflective cell. If a sample is introduced between the mirrors of a Fabry-Perot interferometer, the addition of material results in a perturbation of the cavity and would be observed as a shift and attenuation of the resonance peak. The multipass reflective cell would operate in a similar manner except that only the attenuation would be measured. This can be accomplished by direct measurement of the beam intensity with and without the sample.

The dielectric properties of materials are characterized using well developed techniques as given in Refs. 3 and 4 for polar and non-polar molecules. By the application of an external field, material polarization may occur by electron cloud distortion and/or by dipole orientation. The polarizability may then be related to the susceptibility and index of refraction of the material. Reference 5 lists a variety of methods for determination of elements of the polarizability tensor including molecular refraction, anisotropic light scattering, optical birefringence, and others.

Section II of this study provides the theory for basic dielectric properties as derived from Maxwell's equations. Also included are the basic equations for a Fabry-Perot interferometer and the relations between attenuation and phase shift as related to particle susceptibilities. Section III describes the experimental apparatus used to obtain these measurements. These include aerosol production, evolution of the final multipass reflective cell, and development of the Fabry-Perot interferometer. Section IV is a discussion of the results obtained with a particulate suspension of zinc oxide.

II. THEORY

Dielectric response in a material is due to a charge separation, or permanent dipole orientation, resulting in polarization of a system when an external electric field is applied. This polarization can be linear, in which case the polarization is directly proportional to the electric field, or non-linear in which case the polarization is proportional to a higher power of the electric field. Particle anisotropies result in the proportionality constant being a tensor quantity.

The following theory was developed to relate the polarizability and intrinsic susceptibility (independent of particle shape or size) to the extrinsic susceptibility which can be measured. The theory was expanded to include complex susceptibilities and particles of different geometrical shapes.

Although the experimental verification of the applicability of the proposed method of measurement which is reported here deals only with zinc oxide, the method can easily be applied to a variety of other particulate suspensions.

A. BASIC SUSCEPTIBILITY THEORY

1. Intrinsic Susceptibility

In atomic theory one considers a suspension to be composed of interacting particles embedded in air. If

however the region of measurement is large compared with the dimensions of the particles this region can be considered a continuous medium. Upon interacting with a weak external field E_0 the usual linear relations hold:

$$P = \epsilon_0 \chi E_0 \quad 2.1$$

where P is the polarization, ϵ_0 the permittivity of free space and χ the susceptibility of the medium, and

$$\epsilon = 1 + \chi \quad 2.2$$

where ϵ is the dielectric constant. If however a continuous medium cannot be assumed, but one consisting of discrete particles, an effective field must be considered. This effective field E' acting inside the particle is different from the average field acting over a large number of particles, due to depolarization effects. This is depicted in Fig. 1.

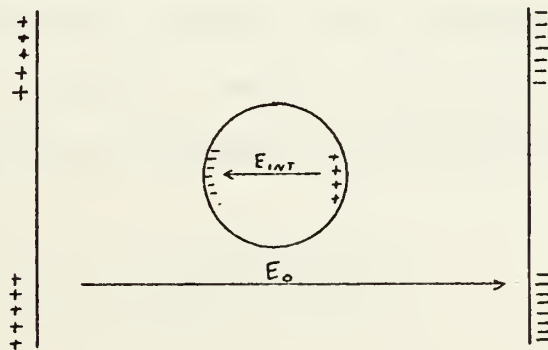


FIGURE 1. PARTICLE EFFECTIVE FIELD

Inside the particle

$$P = \epsilon_0 \chi E' \quad 2.3$$

where χ is the intrinsic susceptibility. Inside the particle $E' \neq E_0$ but is reduced by an amount which is a function of particle geometry. In this case

$$E' = E_0 - LP/\epsilon_0 \quad 2.4$$

where L is the depolarization factor. Substitution of eq. 2.4 into eq. 2.3 and rearranging gives

$$P = \epsilon_0 [\chi/(1+L\chi)] E_0 \quad 2.5$$

Also

$$P/\epsilon_0 E_0 = \chi_e = \chi/(1+L\chi) \quad 2.6$$

where χ_e is the extrinsic susceptibility. Thus one obtains a relation between intrinsic and extrinsic susceptibilities.

If we assume a complex susceptibility $\chi = \chi' - i\chi''$ we get the results obtained by Tolles in Ref. 3:

$$\chi_e' = \frac{\chi' + L(\chi'^2 + \chi''^2)}{(1 + L\chi')^2 + L^2\chi''^2} \quad 2.7$$

$$\chi_e'' = \frac{\chi''}{(1 + L\chi')^2 + L^2\chi''^2}$$

Thus knowing the value of L and measuring χ'_e and χ''_e , as will be described later, the intrinsic susceptibilities can be determined.

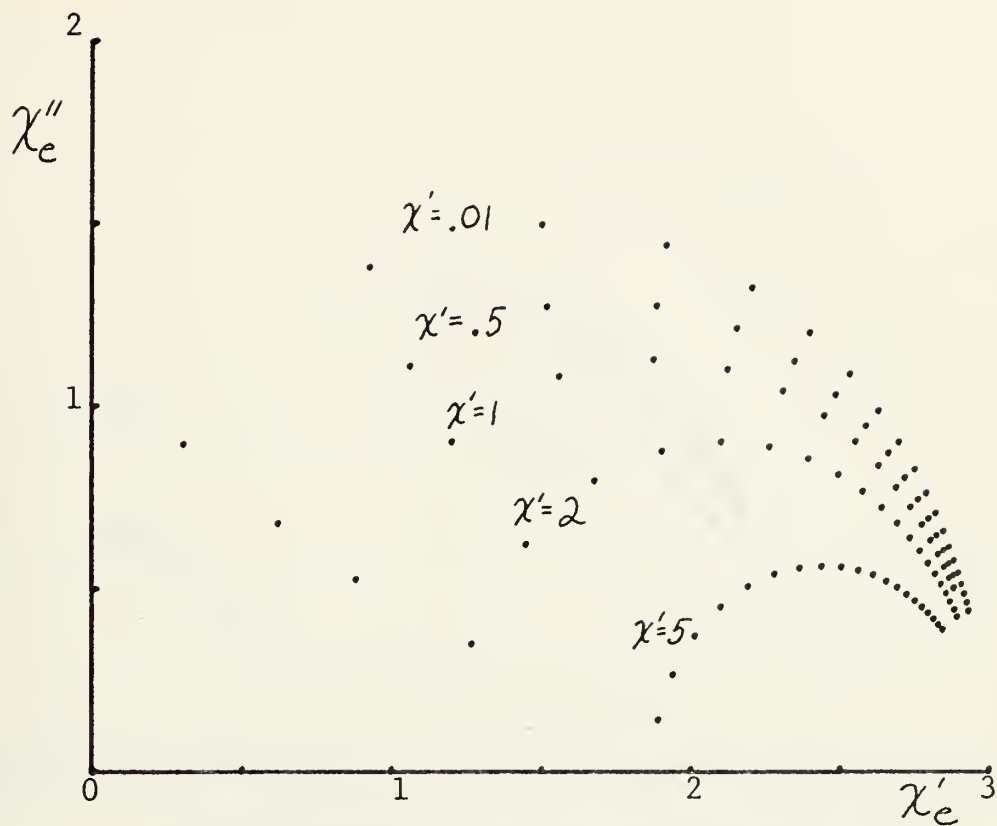
As stated above the depolarization factor is a function of particle geometry and varies with particle dimensions. Under these circumstances eq. 2.7 should more correctly be a sum over L_i where the subscript i refers to the particle x , y , and z directions and the z direction is taken along the long axis of the cylindrical particles. In this case eq. 2.7 becomes

$$\chi'_e = \frac{1}{3} \sum_i \frac{\chi' + L_i (\chi'^2 + \chi''^2)}{(1 + L_i \chi')^2 + L_i^2 \chi''^2} \quad i=1,2,3 \quad 2.8$$

$$\chi''_e = \frac{1}{3} \sum_i \frac{\chi''}{(1 + L_i \chi')^2 + L_i^2 \chi''^2}$$

where $\sum_i L_i = 1$. For spherical particles $L_1=L_2=L_3=\frac{1}{3}$. For ideal infinite rods $L_1=L_2=\frac{1}{2}$ and $L_3=0$. Equation 2.8 is graphed for various values of χ''_e and χ'_e for a sphere (Fig. 2a) and for a rod with $L_1=L_2=.45$ and $L_3=.1$ (Fig. 2b).

Stoner in Table I of Ref. 6 gives values of the demagnetization factors for prolate ellipsoids of revolution in terms of the particle aspect ratio A , where the aspect ratio is the length to diameter ratio. The quantities can



PARTICLE INTRINSIC SUSCEPTIBILITY-SPHERE

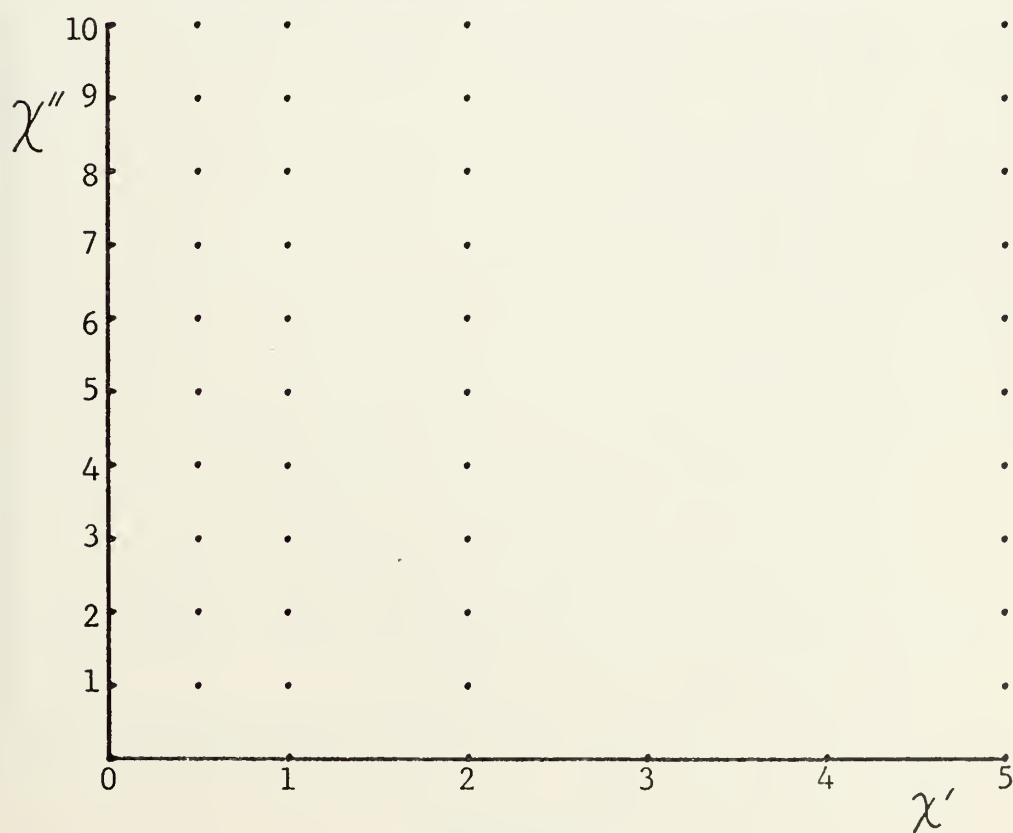
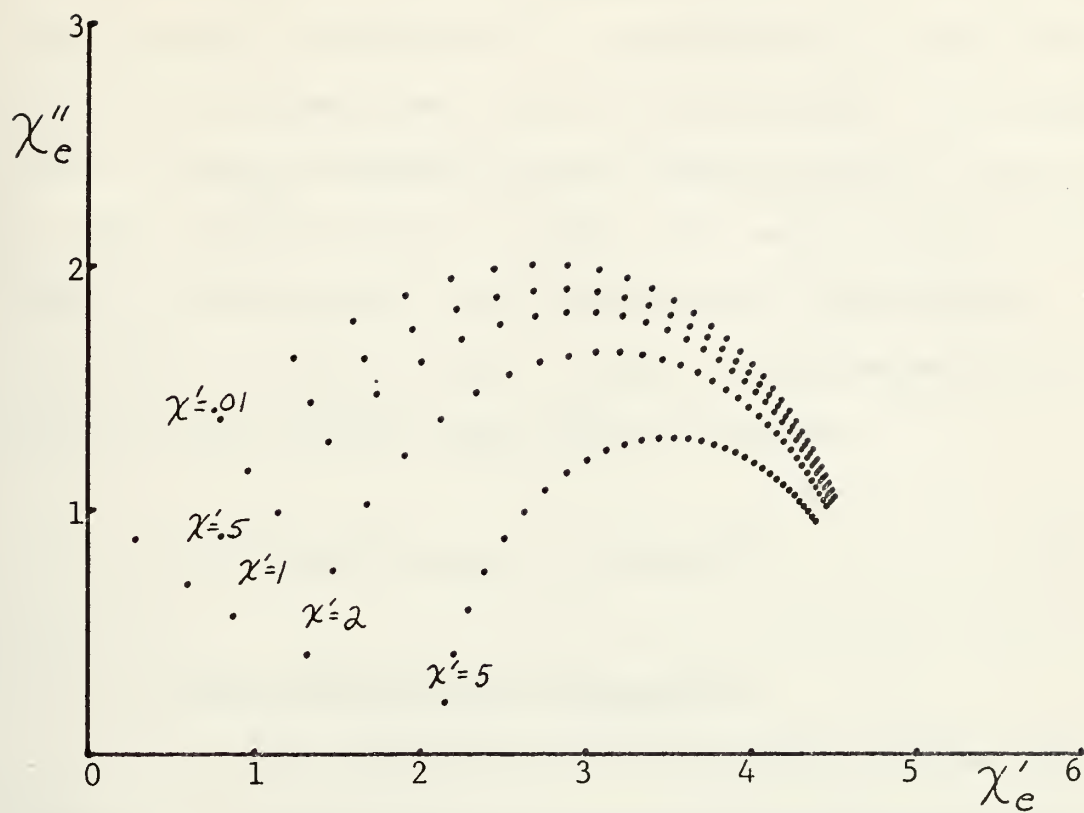


FIGURE 2a



PARTICLE INTRINSIC SUSCEPTIBILITY-CYLINDER

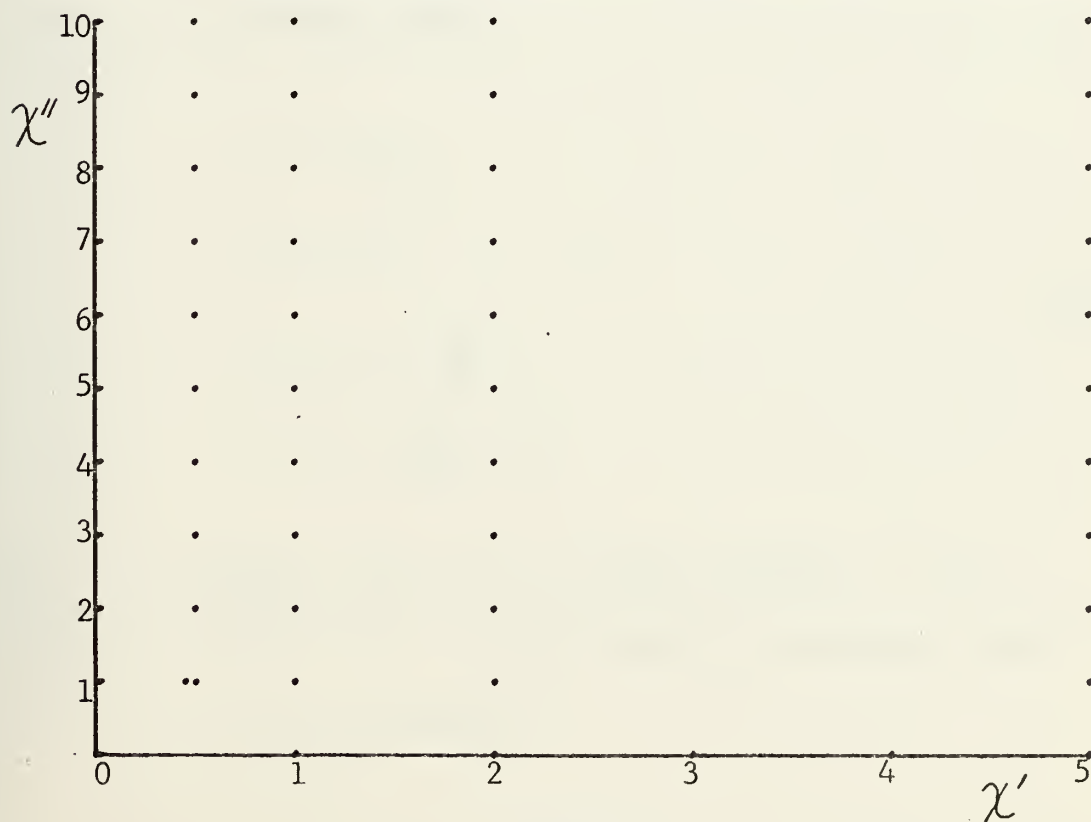


FIGURE 2b

be used directly for depolarization factors for rods since little error is encountered in approximating these rods by ellipsoids if the aspect ratio is high enough. For example, Stoner gives the demagnetization/depolarization factors for an aspect ratio of 20 as $L_1=L_2=.497$ and $L_3=.0067$ which differs only slightly from the ideal rod case stated previously. Tolles in Ref. 3 gives an approximation for the depolarization factor along the rod axis as

$$L_3 = (4.021 \log_{10} A - 0.92) / 2A^2 \quad 2.9$$

2. Susceptibility and Attenuation

One now determines the relationship between the susceptibility and some physically measurable parameter. Maxwell's equations are:

$$\begin{aligned} \nabla \cdot \mathbf{E} &= \frac{\rho}{\epsilon_0} \\ \nabla \cdot \mathbf{H} &= 0 \\ \nabla \times \mathbf{E} &= -\mu \frac{\partial \mathbf{H}}{\partial t} \\ \nabla \times \mathbf{H} &= \epsilon \frac{\partial \mathbf{E}}{\partial t} + \mathbf{j} \end{aligned} \quad 2.10$$

If it is assumed there are no free charges ($\rho = 0$), a material conductivity σ ($\mathbf{j} = \sigma \mathbf{E}$) and a sinusoidal field

$$\mathbf{E} = \mathbf{E}_0 e^{i(\omega t - kz)}$$

the usual wave equation can be obtained with the dispersion relation

$$k^2 = \mu\epsilon\omega^2(1 - i \frac{\sigma}{\epsilon\omega}) \quad 2.11$$

For $\frac{\sigma}{\epsilon\omega} \ll 1$

$$k \approx \sqrt{\mu\epsilon} \omega(1 - i \frac{\sigma}{2\epsilon\omega})$$

Since intensity $I \propto |E|^2 \propto e^{-k\sigma z/\epsilon\omega}$ an attenuation coefficient γ can be related to the conductivity with

$$\gamma = k \frac{\sigma}{\epsilon\omega} \quad 2.12$$

For a linear medium one can write the dielectric constant as

$$\epsilon = \epsilon_0(1 + \chi'_S - i\chi''_S)$$

where the subscript s refers to the overall extrinsic aerosol susceptibility. Substitution of this into eq. 2.11 gives

$$k \approx \frac{\omega}{c} \sqrt{1 + \chi'_S} (1 - i \frac{\chi''_S}{2(1 + \chi'_S)}) \quad 2.13$$

where it is assumed $\frac{\chi_s''}{1+\chi_s'} \ll 1$ and where all imaginary effects have been combined as one χ_s'' . Proceeding as before a relation between attenuation coefficient and susceptibility is found as

$$\gamma = k\chi_s'' \quad 2.14$$

for $\chi_s' \ll 1$. Equation 2.14 shows that if an attenuation coefficient for an aerosol can be determined experimentally the complex part of the aerosol susceptibility can be determined. A method for making this measurement will be described in greater detail.

3. Aerosol Effects

Equation 2.14 can be used to relate the attenuation coefficient to the aerosol susceptibility. If the aerosol were a continuous medium this would be the material susceptibility. Since it is not continuous one must take into account the fact that only a part of the volume is occupied by the material itself. Defining the filling factor f as the fraction of space filled with a dielectric material exhibiting a single particle extrinsic susceptibility χ_e gives

$$\chi_s = f\chi_e .$$

With no externally applied electric field the particles are randomly oriented so that in any one direction eq. 2.14 becomes

$$\gamma \simeq k \frac{f}{3} \chi_e'' \quad 2.15$$

Thus, by using polarized monochromatic light and assuming that the only contribution is due to particles aligned along the axis of polarization, eq. 2.15 relates the measured attenuation of a beam to the particle susceptibility.

This can be converted to a more convenient expression in terms of an attenuation cross section σ_c . If the initial intensity of the light source without the aerosol is I_0 then the measured intensity with the aerosol will be

$$I = I_0 e^{-\gamma z} = e^{-\sigma_c N z} = e^{-\frac{\sigma_c}{V} N V z} \quad 2.16$$

where N is the number of particles per unit volume, V the volume occupied by these particles and z is the effective length the beam has gone through the aerosol. Since $NV = f$, eq. 2.16 leads to an attenuation cross section per unit volume of

$$\frac{\sigma_c}{V} = \frac{1}{fz} \ln \frac{I_0}{I} \quad 2.17$$

B. MULTIPASS REFLECTIVE CELL

1. Basic Theory

The multipass reflective cell uses light reflection off coated surfaces to achieve large distances in relatively short laboratory spaces. Two general types of designs can be used. The first is two plane flat, coated mirrors placed parallel to each other a certain distance apart as shown in Fig. 3

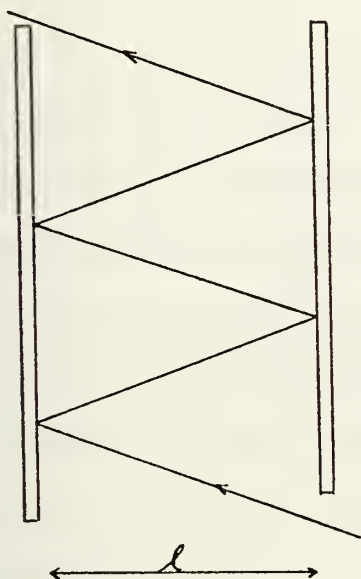


FIGURE 3

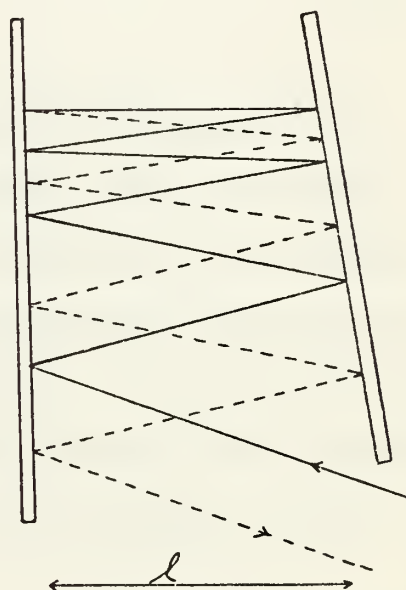


FIGURE 4

MULTIPASS REFLECTIVE CELL DESIGNS

The incoming light is reflected off each plate at an angle θ until it emerges at the other end. The only losses of light intensity are those at each mirror due to the reflectivity R being <1 and in the air between the plates. Born and Wolf in Ref. 7 give an expression for the intensity reflection coefficient from a metallic surface as

$$R = \frac{\frac{2\sigma}{\nu} + 1 - 2\sqrt{\sigma/\nu}}{2\frac{\sigma}{\nu} + 1 + 2\sqrt{\sigma/\nu}} \quad 2.18$$

where ν is the frequency of the light and σ is the conductivity. When ν/σ is sufficiently small this may be expanded in a power series of $\sqrt{\nu/\sigma}$ to obtain

$$R \approx 1 - 2\sqrt{\nu/\sigma} + \dots \quad 2.19$$

Equation 2.19 shows that for increasing wavelength the reflection coefficient approaches unity. This means any multipass reflective cell set up to operate in the visible will operate with less loss in the infrared. This principle was used in the design of the final cell. The total distance traveled by the beam is $z = (2n+1)\ell$ where n is the number of reflections on mirror 1 and ℓ is the distance between the mirrors.

The second type of reflective cell design is one in which the mirrors are not parallel to each other but at an angle as depicted in Fig. 4. This design has the effect of returning the beam to its initial point after traversing a distance along the mirrors. An advantage of this design is the fact that shorter mirrors can produce the same path length as the previous design.

Due to diffraction effects, the laser beam will tend to spread while traversing the cell leading to beam

overlap at the mirrors. An estimation of the mirror length necessary to avoid beam overlap can be made beginning with Fig. 5. As seen in Fig. 5

$$\begin{aligned}
 Y_1 &= \ell \sin \phi \approx \ell \phi \\
 Y_2 &= \ell \sin \phi \approx \ell \phi \\
 Y_3 &= \ell \sin(\phi - \Delta) \approx \ell(\phi - \Delta) \\
 Y_4 &= \ell \sin(\phi - \Delta) \approx \ell(\phi - \Delta) \\
 &\vdots
 \end{aligned}$$

and the total distance along mirror 2 is

$$Y_T = \ell \phi + \ell \phi + \ell(\phi - \Delta) + \ell(\phi - \Delta) + \ell(\phi - 2\Delta) \dots$$

If n is the number of bounces the beam makes on mirror number two then

$$Y_T = \ell(2n-1)\phi - \sum_1^n \ell(2n-3)\Delta \quad 2.20$$

Evaluating the sum gives

$$\sum_1^n \ell(2n-3)\Delta = \ell(n-1)^2 \Delta$$

Equation 2.20 now becomes

$$Y_T = (2n-1)\phi - \ell(n-1)^2 \Delta \quad 2.21$$

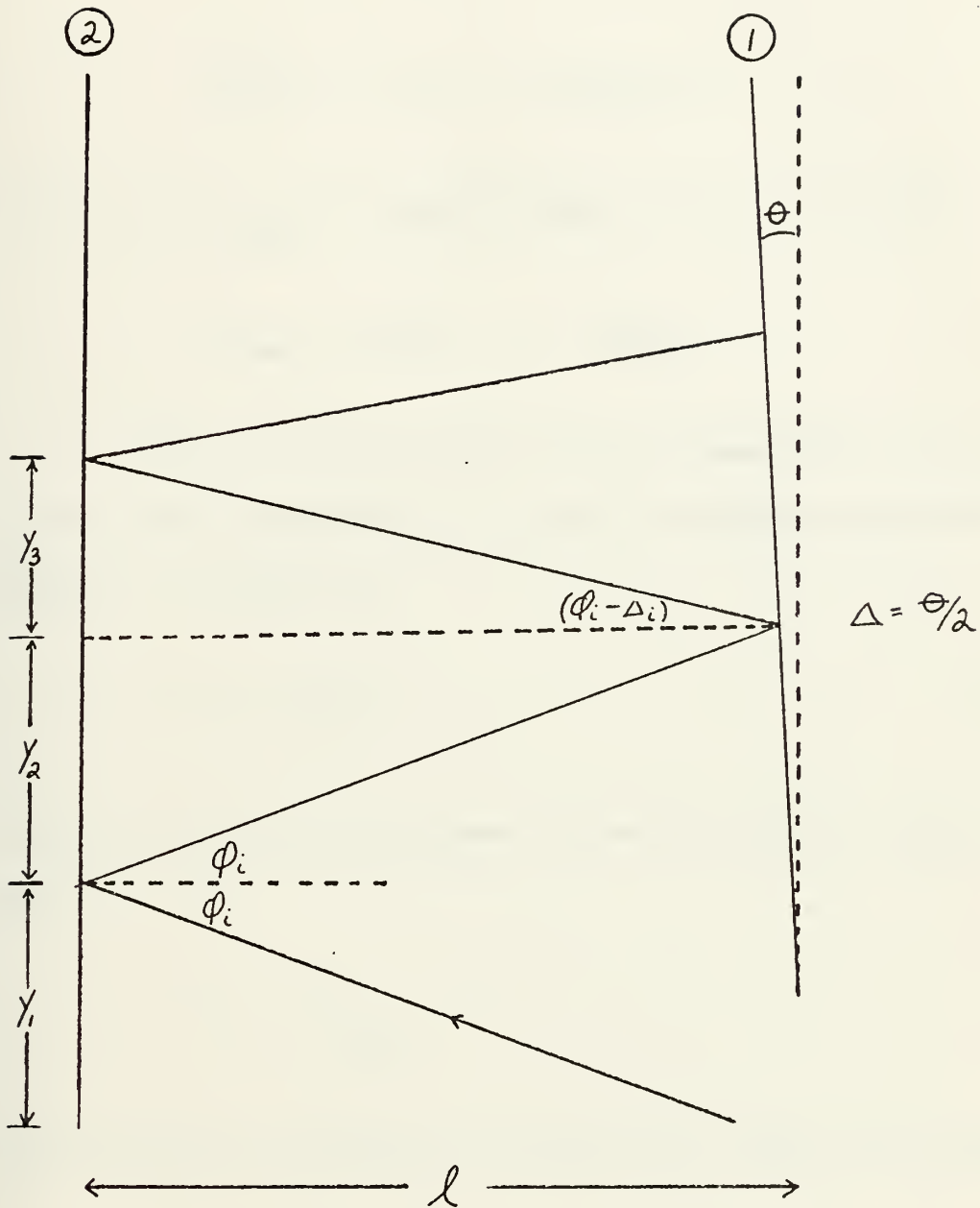


FIGURE 5
DETERMINATION OF MINIMUM MIRROR
LENGTH FOR MULTIPASS REFLECTIVE CELL

The maximum traversal, Y_{\max} , along the mirror is obtained by taking the derivative of equation 2.21 with respect to n to obtain

$$\frac{dY_T}{dN} = 0 = 2\ell\phi - \ell\Delta 2(N_{\max}-1)$$

Solving for N_{\max} and substituting in eq. 2.21 gives

$$Y_{\max} = \ell\phi\left(\frac{\phi}{\Delta} + 1\right) = \ell\phi N_{\max}$$

If one now examines a total traversal of the beam up and down the mirrors, the total distance traveled by the beam, z , is given by

$$z = 2N_t\ell \tag{2.23}$$

where N_t is the total number of reflections on mirror 2 and

$$N_t \approx 2N_{\max} \tag{2.24}$$

Substitution of equation 2.24 and 2.23 into 2.22 yields

$$Y_{\max} = \frac{z}{4} \phi \tag{2.25}$$

Equation 2.25 gives an expression for the maximum distance the beam travels along the mirror or, in effect, the minimum mirror length necessary in the experiment as a function of the total distance traveled by the beam and the angle ϕ . A restriction must now be put on ϕ in relation to the divergence of the beam. To prevent overlap of the beam at the last two reflections, the distance between the reflections must be greater than the diverged beam diameter or

$$\text{distance between reflections} > 2Y_1 = 2\ell\phi$$

Also, at a distance z , the beam diameter $d(z)$ is

$$d(z) = d_0 + 2Dz$$

where D is the divergence and d_0 is the initial beam diameter. In the diffraction limited case

$$\sin \theta \approx \theta = D = 1.22 \frac{\lambda}{d'}$$

where d' is the diameter of the diffracting aperture.

Using the above restrictions the limit on ϕ is

$$\theta \approx \frac{Dz}{\ell} \tag{2.26}$$

which results in a maximum traversal of

$$Y_{\max} = \frac{Dz^2}{4\ell} \quad 2.27$$

Equation 2.27 gives an expression for the minimum length mirror in terms of measurable quantities. For example, for $z = 15$ ft, $\ell = 20$ cm. and the divergence as a result of a plane wave laser source passing through a 4 mm aperture, $Y_{\max} = 5.3$ in.

2. Perturbation Effects

Introduction of a sample between the plates of the cell results in a perturbation of the cavity. The zinc oxide particles in random orientation cause an attenuation of the incoming beam due to absorption. Scattering will also result in beam attenuation but it is considered small compared to absorption and will be ignored. If the beam intensity is monitored with a detector then a change in the output will occur when zinc oxide is introduced. If the relative magnitudes of the intensities are recorded then the $\ln(I_0/I)$ term of equation 2.17 can be determined. The total distance Z traveled by the beam is determined from the number of beam maxima appearing at the detector. These maxima will appear as alternately bright dots then dark non-transmission spaces at the detector. If the n^{th} dot is on the detector then

$$Z = (2n-1)\ell$$

where ℓ is the distance between the mirrors. Here it is assumed that the tilt of the mirror causes a negligible change in ℓ at the mirror ends as compared to the center of the mirror.

The only remaining term to be determined is the filling factor f . This may be done experimentally or approximated from the stoichiometry involved in producing a particulate suspension. With the intensity ratios, the total distance and the filling factors, an extinction cross section per unit volume can be determined.

In the case where scattering is comparable to or greater than absorption a distinction must be made between scattering and absorption cross sections. Lind and Greenberg in Ref. 8 give extinction and scattering efficiencies for obliquely oriented cylinders. The beam attenuation will be the result of the addition of these two cross sections.

C. FABRY-PEROT INTERFEROMETER

1. Basic Theory

In layman's terms a Fabry-Perot interferometer is a device consisting of two partially transmitting, reflective surfaces. Light entering the device is reflected back and forth with successive beams interfering, resulting in a circular interference pattern at the output. The reflecting surfaces can either be plane or curved mirrors, the latter being the only type considered in the following development.

The basic design for a spherical mirror Fabry-Perot interferometer is shown in Fig. 6. It consists of two identical curved mirrors separated a distance equal to their common radii of curvature. As can be seen from Fig. 6 there are two types of exiting rays, those which have traveled a distance $4m\ell$ and those traveling a distance $(4m+2)\ell$, where m is any integer and the 0^{th} order is taken where the first ray of type I exits the output mirror. Hercher in Ref. 9 gives the expressions for the patterns produced in the central plane of the interferometer as

$$\text{TYPE I} \quad I_1 = I_0 \left[\frac{T'}{1-R'} \right]^2 \left\{ 1 + \left[\frac{2R'}{1-R'^2} \right]^2 \sin^2 \frac{\delta}{2} \right\}^{-1} \quad 2.28$$

$$\text{TYPE II} \quad I_2 = (R')^2 I_1$$

where

$$\delta = \frac{2\pi}{\lambda} [\Delta(\rho) + 4(r+\epsilon)]$$

and T' is the mirror transmissivity, R' the mirror reflectivity, $\Delta(\rho)$ the path difference, and ϵ is the difference between the Fabry-Perot mirror separation and the confocal spacing r . Hercher also shows that bright fringes are formed in the central plane of the interferometer for the condition

$$\delta = 2m\pi$$

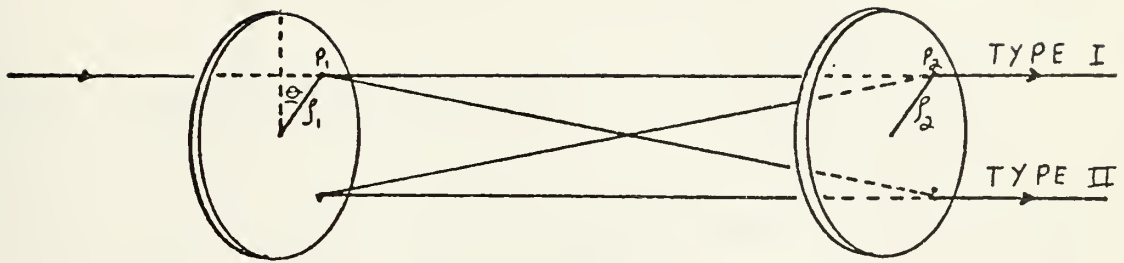


FIGURE 6
BASIC INTERFEROMETER DESIGN

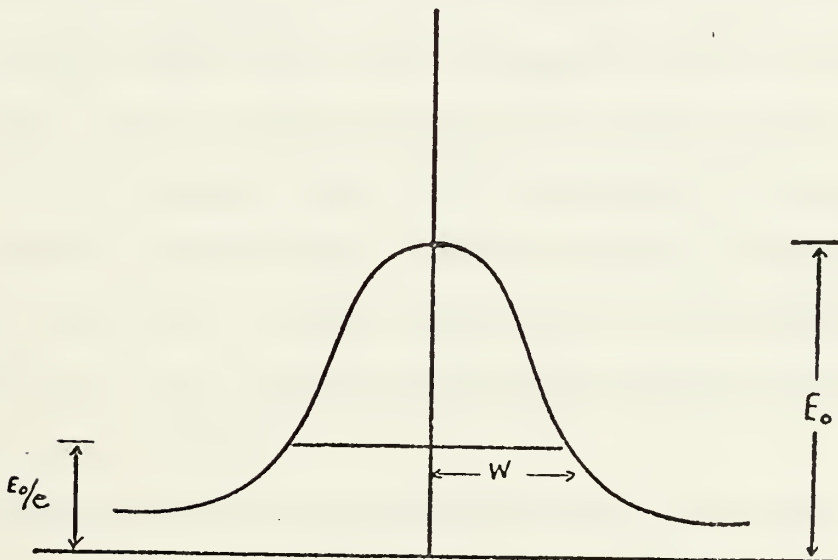


FIGURE 7
BEAM RADIUS

Thus,

$$\frac{\rho^4}{r^3} + 4\epsilon \frac{\rho^2}{r^2} = m\lambda \quad 2.29$$

with a fringe radius given by

$$\rho_m = [-2\epsilon r \pm (4\epsilon^2 r^2 + m\lambda r^3)^{1/2}]^{1/2} \quad 2.30$$

Thus the result is a circular interference pattern.

The equipment used in this study was a slight modification of that described above. A scanning spherical mirror interferometer (SSMI) was used. This is one in which one of the mirrors is held fixed and the second can be moved laterally along the axis of the interferometer. If it is assumed that the axis of the interferometer and the incoming light coincide, then the axial resonance of the interferometer occurs each time the separation between the mirrors is $q\lambda/2$ where q is an integer, and λ the wavelength of the incoming light. As the second mirror scans a spatial distance, each time this condition is met a resonance is encountered and the intensity of the light transmitted through the interferometer is a maximum.

The resonance condition $q\lambda/2$ holds strictly for axial modes. There can also exist transverse modes. If one defines the word mode to mean a well defined spatial distribution of electro-magnetic fields between the mirrors then

the modal field along the optic axis (z axis) of the interferometer at resonance is that of a standing wave. If one further defines n, m, q as the number of nodes in the x, y, z direction respectively then Fork, Herriot and Kogelnik in Ref. 10 give the equation for the resonant wavelength of the cavity as

$$\frac{2\ell}{\lambda} = q + \frac{1}{\pi} (1+m+n) \cos^{-1}(1 - \frac{\ell}{R}) \quad 2.31$$

where R is the radius of curvature of the mirrors. In this study only the fundamental modes in the transverse direction will be considered in which case $m = n = 0$. For this condition Yariv in Ref. 11 gives a simpler form of the resonant condition as

$$\frac{2n\ell \cos \theta}{\lambda} = q \quad 2.32$$

where q is an integer, ℓ the distance between mirrors, and n the index of refraction of the medium. Since the light is incident along the optic axis, $\cos \theta \approx 1$. In this fundamental mode the transverse field distribution is approximately Gaussian, as shown in Ref. 10, and most of the power is distributed near the axis. A reference dimension can then be defined as the "beam radius," W , which is the $1/e$ radius of the electric field as shown in Fig. 7. All terms and quantities can now be described in terms of this beam radius.

If the central fringe of the interference pattern is fed into a detector and then to an oscilloscope the standard Fabry-Perot intensity resonance pattern as shown in Fig. 8 will be observed as the movable mirror is scanned across the resonances. The horizontal axis is proportional to the distance the mirror has moved. From Fig. 8 a new term, the cavity finesse F , can be defined, which is a measure of the resolution of the interferometer. The resolution is the ability to distinguish between two separate, adjacent, resonance peaks. The finesse is the quantity which is of the most interest in this study. Knowing the initial cavity finesse and observing any shifts in the resonances, as will be described later, will lead to susceptibility determinations.

The cavity finesse is defined as

$$F = \frac{\Delta\omega}{\delta\omega_0} \quad 2.33$$

As can be seen the better the cavity or, in other words, the better the finesse the sharper the resonance peaks will be and the better the cavity resolution will be. The values ω_0 and ω'_0 are adjacent cavity modes and are related in that ω_0 solves eq. 2.32 for q and ω'_0 solves the same equation for $q+1$. Yariv in Ref. 11 relates the finesse to the mirror reflectivity as

$$F = \pi \sqrt{R}/(1-R)$$

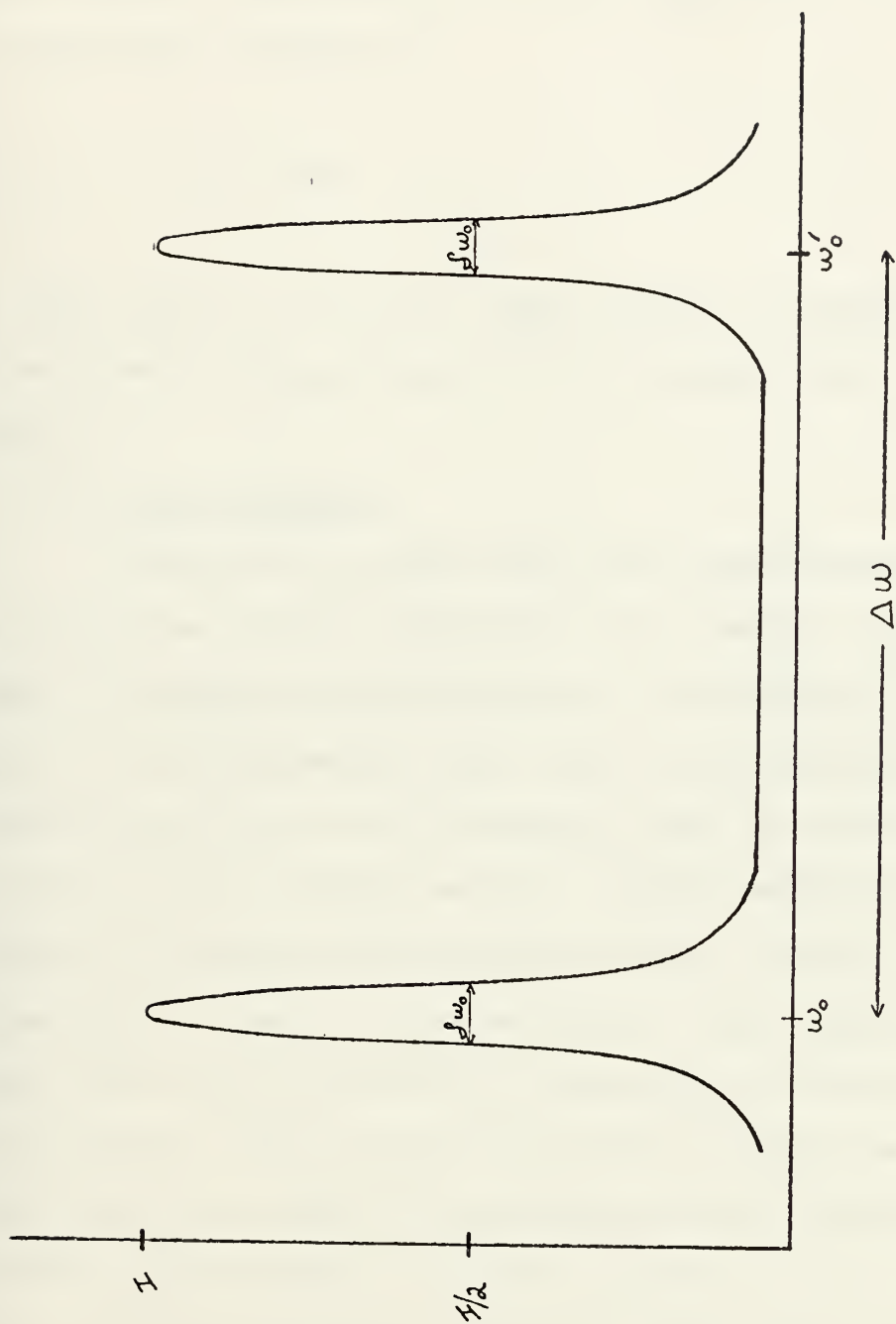


FIGURE 8
CAVITY FINESSE

In reality this is only an approximation. It is valid only in the limit of perfectly smooth mirrors. For mirrors with surface irregularities on the order of λ/m the limit on attainable finesse is

$$F = m/2 \qquad 2.34$$

As seen from eq. 2.34 if a high finesse is desired mirrors of extremely high quality must be obtained which can be costly.

2. Mode Matching

Equation 2.31 shows that the interferometer response is a function of the transverse mode numbers n and m . In order to facilitate measurements it is necessary to work only in the fundamental mode, which is accomplished by insuring the axis of the incoming light is coincident with the axis of the interferometer. Another method for efficient coupling and increased finesse, should it be necessary, is that of mode matching. This occurs when the beam radius and the radius of curvature of the wavefront of the incoming light at the input mirror exactly match the beam radius and radius of curvature of the fundamental mode of the interferometer. If this condition is not met exactly then some power is fed into higher order modes and the fundamental mode is reduced accordingly.

Figure 9 shows the beam envelope inside the Fabry-Perot. W_0 , called the beam waist, is the minimum beam

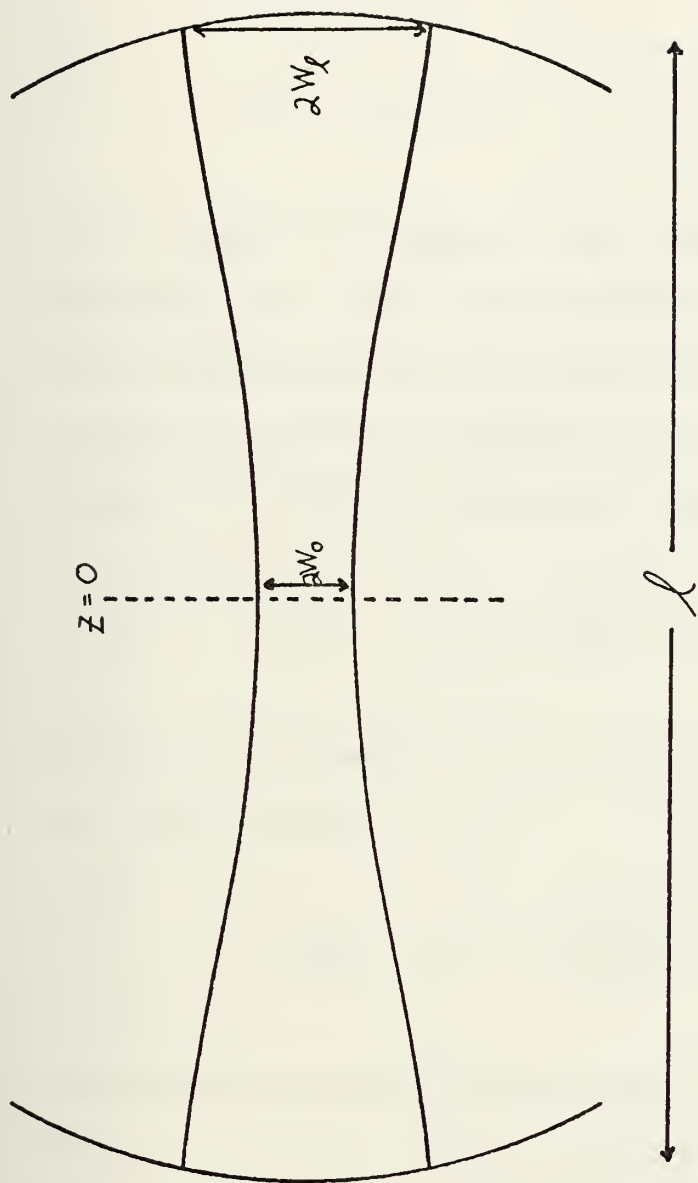


FIGURE 9

BEAM WAIST

radius. W_ℓ is the beam width at the mirrors. Yariv in Ref. 11 gives these values for a symmetrical confocal resonator as used in this study as

$$W_0 = \left[\frac{\lambda \ell}{2\pi} \right]^{1/2} \quad 2.35$$

$$W = \sqrt{2} W_0$$

As an example for mirrors with radii of curvature of 20 cm. the beam waist for 10.6 μ m radiation becomes $W_0 = .058$ cm. and the beam dimensions at the mirrors are $W_\ell = .082$ cm. Yariv also gives the equation for the radius of curvature of the wavefronts at any point z as

$$R(z) = z \left[1 + \left(\frac{\pi W_0^2}{\lambda z} \right)^2 \right]$$

which in the symmetrical confocal case at the mirrors ($z = \ell/2$) becomes

$$R\left(\frac{\ell}{2}\right) = \frac{\ell}{2} \left[1 + \left(\frac{2\pi W_0^2}{\lambda \ell} \right)^2 \right] \quad 2.36$$

By making the beam dimensions at the input mirror correspond to eq. 2.35 and 2.36 mode matching is accomplished.

If the power transmitted in the fundamental mode is T_0 then for non-matched conditions this is reduced to κT_0 , where κ is the input coupling coefficient and is given by Fork, Herriott and Kogelnik in Ref. 10 as

$$\kappa = \frac{4}{\left[\left(\frac{W}{\bar{W}} + \frac{\bar{W}}{W} \right)^2 + (\sigma')^2 \frac{\bar{W}^2}{W^2} \left(\frac{R}{\bar{R}} - 1 \right)^2 \right]} \quad 2.37$$

The bar over a letter refers to a beam quantity and the letter without a bar indicates an interferometer quantity. σ' is a system parameter

$$\sigma' = \left(\frac{\pi W^2}{\lambda R} \right)$$

If the curvature mismatch is unavoidable, better coupling is achieved for an incoming beam radius less than the fundamental radius. This is shown in Fig. 6 of Ref. 10 by graphing κ vs. $\left(\frac{\bar{W}}{W} \right)^2$ and examining the maximum values for $\frac{\bar{W}}{W} < 1$.

3. Cavity Perturbations

When a sample is introduced between the mirrors of the Fabry-Perot a perturbation results whereby the resonance peaks of Fig. 9 are shifted and attenuated as shown in Fig. 10. Here $\Delta\omega_0$ is the phase shift due to the sample and I_0 is the attenuation.

Lax and Button in Ref. 12 give an expression for the real part of the susceptibility (χ'_e) in terms of the frequency shift as

$$\frac{\Delta\omega_0}{\omega_0} = - \frac{1}{2} \frac{\int \chi'_e E^2 dv}{\int E^2 dv}$$

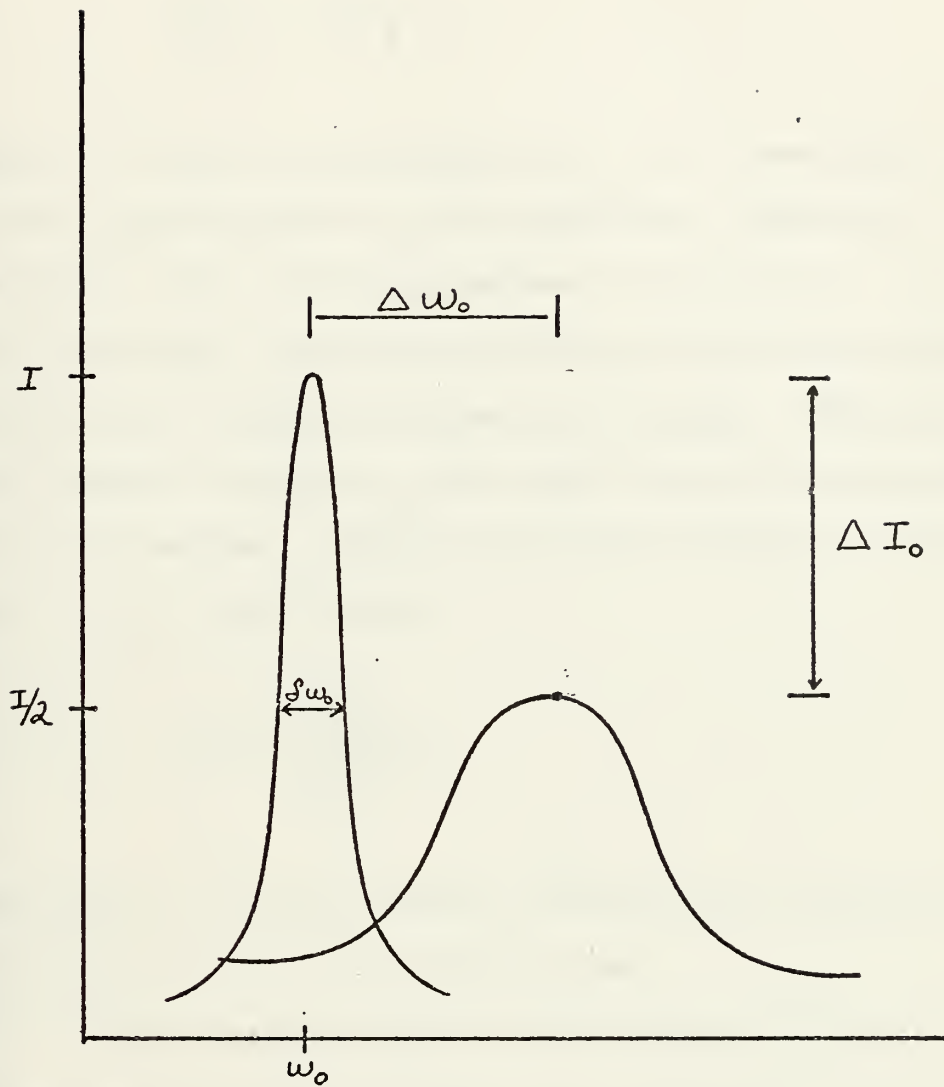


FIGURE 10
CAVITY PERTURBATION EFFECTS

For the one dimensional case with no externally applied electric field this reduces to

$$\frac{\Delta\omega_o}{\omega_o} = - \frac{1}{2} \frac{f}{3} \chi'_e S \quad .2.38$$

where f is the filling factor and S is a term which enters in this study because in the design the sample did not completely fill the space between the mirrors. S is equal to the distance the beam traveled in the sample divided by the total distance between the mirrors. Thus by measuring the frequency change $\Delta\omega_o$ the real part of the susceptibility can be determined. Making the substitutions for the finesse and $\omega'_o - \omega_o = \pi c/\ell$ then

$$\chi'_e = \frac{3\Delta\omega_o \lambda}{\delta\omega_o F \ell f S} \quad 2.39$$

again where ℓ is the distance between the mirrors and λ is the wavelength of the incoming beam.

The imaginary part of the susceptibility can be determined from Eq. 2.15 once the attenuation cross section, Eq. 2.17, is determined. By measuring the heights of the resonance peaks of Fig. 10 with and without the sample, $\ln(I_o/I)$ in Eq. 2.17 can be determined. The only term left to know is Z , the total distance traveled by the beam. Going back to Eq. 2.33 for the finesse, Yariv in Ref. 11

gives an expression for $\Delta\omega$ considering ω_0 and ω'_0 are consecutive modes, and normal incidence as

$$\Delta\omega = \frac{2\pi c}{2\ell} \quad 2.40$$

since $f = \frac{\Delta\omega}{\delta\omega_0}$ this reduces to

$$\delta\omega_0 = \frac{\pi c}{\ell F} \quad 2.41$$

Yariv in Ref. 11 also gives the cavity quality factor Q as

$$Q = \omega_0 t_c = \frac{\omega_0}{\delta\omega_0} \quad 2.42$$

where t_c is the cavity decay lifetime. The total length traveled by the beam, Z , is

$$Z = ct_c = v\lambda \frac{Q}{\omega_0} = \frac{\ell Q \lambda}{2\pi} \quad 2.43$$

Substitution of Eq. 2.41 and 2.42 into 2.43 yields

$$Z = \frac{\ell \omega_0 F \lambda}{2\pi^2 c} = \frac{F \ell}{\pi} \quad 2.44$$

Equation 2.44 now gives an effective path length of the beam in terms of the cavity finesse and the distance between the mirrors which can be measured, and hence χ_e'' can be determined from Eq. 2.15 and 2.17.

D. SUMMARY

In order to better understand the theory developed a brief summary is presented here. For the multipass cell if the intensity of the output beam is measured with and without the sample the ratio I_0/I can be determined. By counting the number of reflections n , passing across the face of the detector, the total distance traveled by the beam is $Z = (2n-1)\ell$. Knowing these values and the filling factor, Eq. 2.17 gives the attenuation cross section per unit volume. From Eq. 2.15 and Eq. 2.16 χ_e'' can be determined.

For the Fabry-Perot interferometer the quantity first needed is the finesse. By measuring the distance between the resonance peaks, $\Delta\omega$, and the halfwidth, $\delta\omega_0$, of the peak, Eq. 2.33 gives the finesse. By measuring the peak heights with and without the sample I_0/I can be determined. The total path length in the sample is then given by Eq. 2.44, and the filling factor is found the same as previously described. Again Eq. 2.17 gives the attenuation cross section and χ_e'' is found as described above. For χ_e' the amount the resonance peak has shifted is measured. Knowing this value and S , the ratio of the distance traveled in the sample to the total distance traveled by the beam, Eq. 2.39 gives the value of χ_e' .

Once the values of χ_e' and χ_e'' are known the values of the intrinsic susceptibility are determined from Eq. 2.8. Since Eq. 2.8 consists of a set of coupled equations they must be solved graphically or numerically.

III. EXPERIMENTAL

In order to provide a clear understanding of the several components of the experimental apparatus this section is divided into four parts: 1) Sample preparation - this will give all applicable parameters necessary to produce a suspension of zinc oxide, 2) Experimental procedure - this part gives an overview of how the apparatus was used without giving exact physical details of each particular item, 3) Multipass reflective cell and Fabry-Perot designs and 4) Supporting experimental apparatus. These last two parts give a detailed description of each piece of equipment. It is hoped that the above order of presentation will give a clear logical progression as to how the final design of this study's proposed method of measurement evolved.

A. SAMPLE PREPARATION

The method of sample preparation here is the same as described by Tolles in Ref. 3 and Fritz in Ref. 13. A single composition of reagent grade zinc oxide in a tubular core was used to produce zinc oxide particles in the vapor phase. The cores were produced from 150-200 gms. of reagent grade zinc oxide which was packed into a hollow coaxial cylinder. This cylinder was then placed in a furnace and sintered at 900 °C for about four and one half hours to produce the hard brittle core used here. References 3 and

13 also describe the preparation of an Indium doped sample core but this doped type core was not used in this study.

The suspension of zinc oxide particles was produced in a Lindberg/Heaviduty furnace at a temperature of 1225 °C. The core was placed in the center of the furnace by slowly inserting it from one end, without touching the furnace tube, which allowed the core to be warmed without cracking the furnace tube. Once the zinc oxide core was positioned properly, hydrogen gas mixed with a carrier gas of nitrogen, was passed over the core. The hydrogen gas reduced the zinc oxide releasing metallic zinc vapor. The zinc vapor was then oxidized to zinc oxide particles. This was accomplished by flowing oxygen through a pyrex tube which passed through the center of the core as shown in Fig. 11. Thus the zinc vapor is oxidized downstream of the core. The nitrogen gas was required as a carrier to provide the flow of particles out the oven and into the measurement cavities.

One end of the furnace tube, which was a 1-5/8 in. mullite tube, was sealed with an asbestos wrapped teflon stopper. The stopper had two holes cut in it, one to provide the hydrogen and nitrogen flow and the second for the oxygen via the pyrex tube. The other end of the tube was connected to a second mullite tube via asbestos and a hose clamp. This second tube was connected similarly to a short third piece which led into the measurement cavity. The reason for the three tube sections was two fold. The first was that

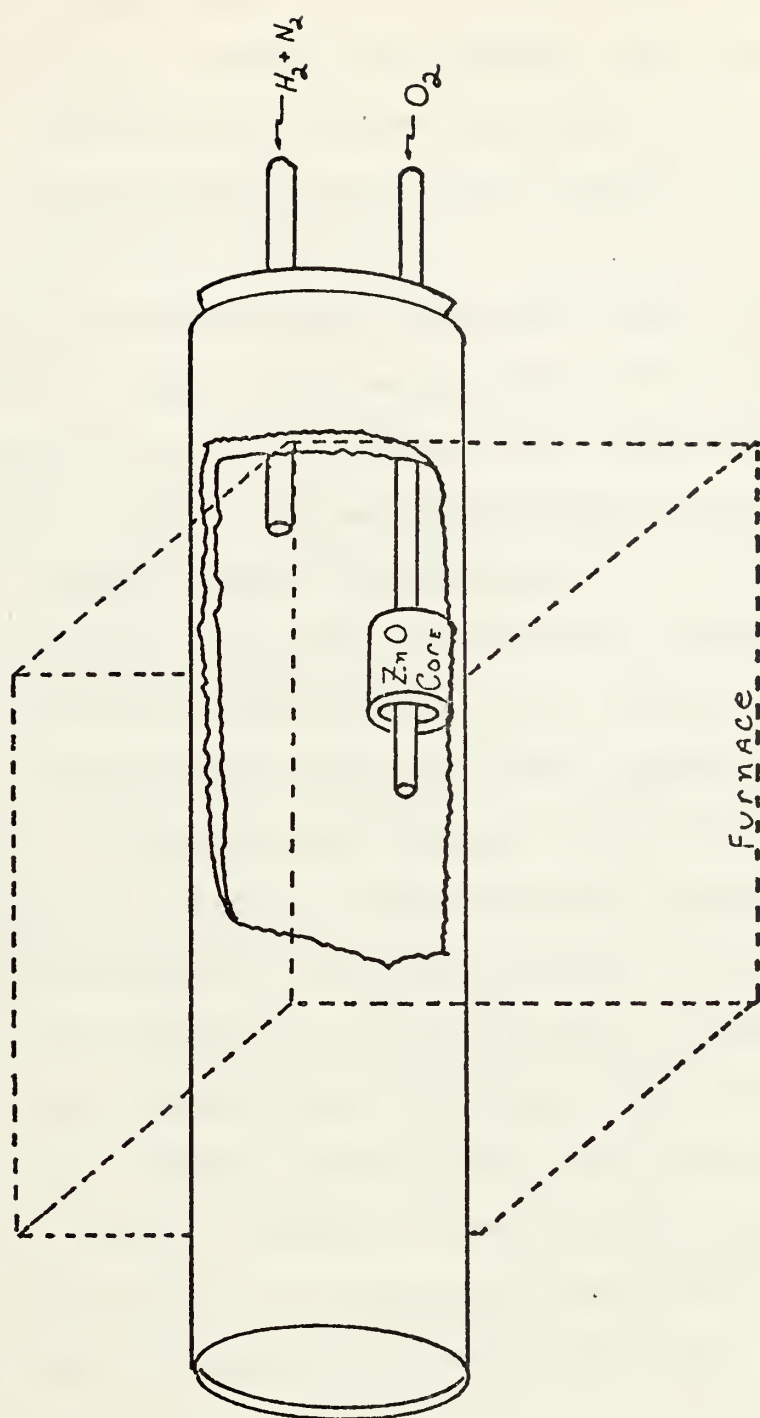


FIGURE 11
SAMPLE PREPARATION

the oven was higher than the cavity. By using three pieces the sample could be directed horizontally into the measurement cavity. The second and most important reason was to insure that the produced particles had reached room temperature prior to entering the cavity.

The initial step in making the sample was to warm the oven to 1225° C. This was done in increments of about 200° C per hour beginning with the minimum oven temperature of 500 °C. The nitrogen gas line was divided in two. One was used as the carrier gas for the hydrogen and the second was used for the cavity protective curtains as will be described later. Both flow rates were set at 8 cu. ft./hr. The oxygen and hydrogen flow rates were then increased to about .2 cu. ft./hr. Since the flow meters used in this study were calibrated for oxygen, the flow rate of the hydrogen has to be multiplied by a conversion factor of 2.4 to account for the difference in gas viscosity. Approximately 30 seconds after the hydrogen and oxygen were turned on a white smoke was observed entering the cavity and measurements could then be taken. Because of the density of the smoke the cavity was placed in a ventilating hood with the lasers and other supporting equipment outside the hood.

B. EXPERIMENTAL PROCEDURE

1. Multipass Reflective Cell

Figure 12 shows a block diagram of the multipass reflective cell apparatus. Once the oven had reached an

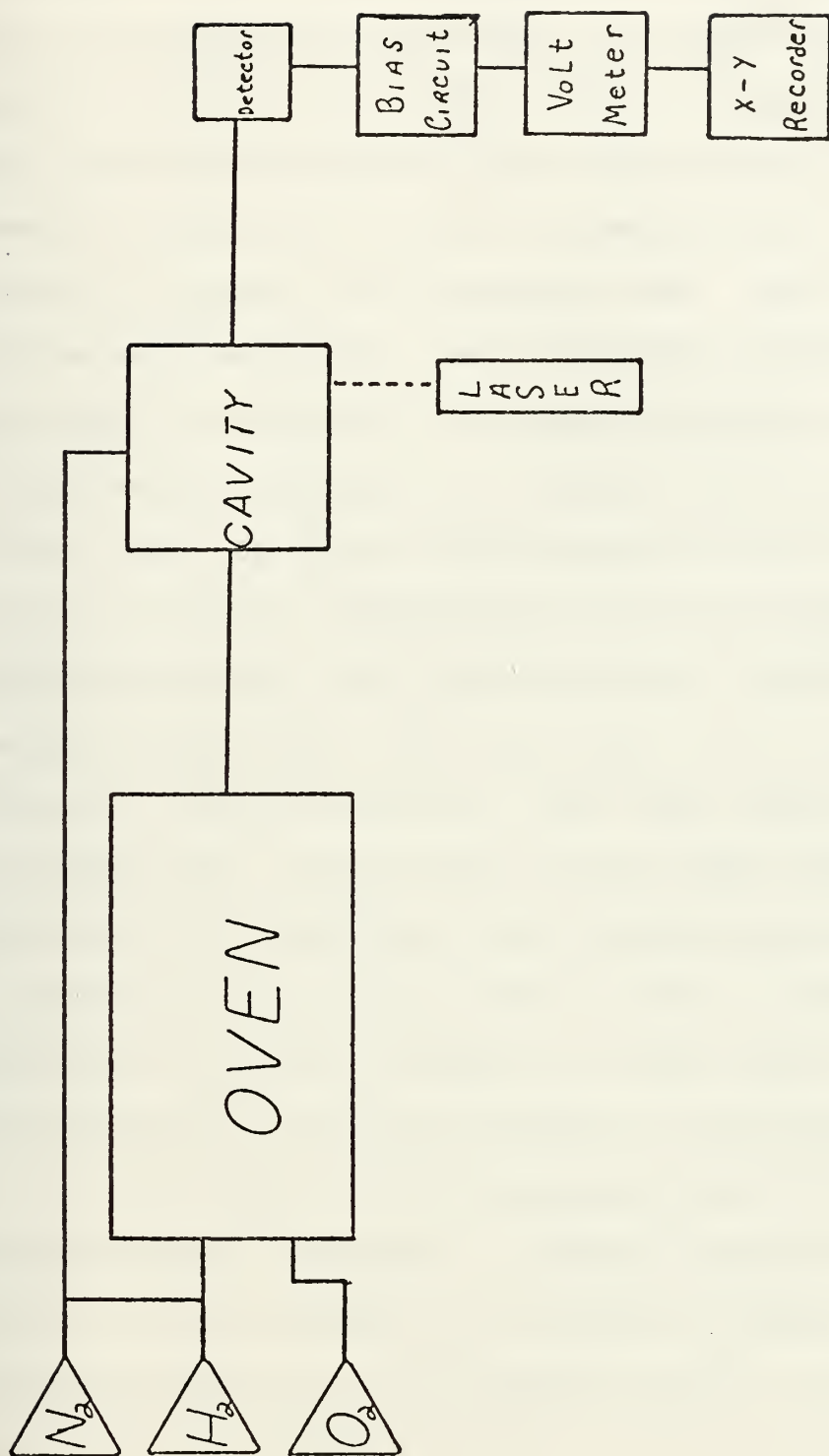


FIGURE 12
BLOCK DIAGRAM
MULTIPASS REFLECTIVE CELL

equilibrium temperature the next step was to align the cell. This was done with a He-Ne laser. The beam entered the hood through a hole and was reflected off two mirrors to bring it up to the height of the cavity. By adjusting these two mirrors the beam was passed through a hole in the side of the cavity and struck the flat fixed cavity mirror. The second cavity mirror was on a gimble mount allowing movement around a vertical and horizontal axis. When not in proper adjustment vertically, the reflections resulted in a pattern as shown in Figure 13a. By proper adjustment the parabolic shape could be reduced to a straight line as shown in Figure 13b. By moving the horizontal tilt a greater number of dots could be observed with the dots extending further along the mirror. The total distance Z could be varied by adjusting this tilt. In this study 6 to 14 dots were used, giving a Z of 97 to 437 cm. The final return dot was reflected off a small output mirror which enabled it to be focused onto a detector. The focusing was accomplished by a spherical mirror with a focal length of about 5 cm. A thermopile detector encased in a metal case to reduce outside electromagnetic noise was placed at the focus of the mirror.

In order to reduce long term time variations, the input beam was "chopped." A chopper consisting of a circular piece of thin aluminum 4 1/2 inches in diameter, which was quartered and two of the quarters cut out, was used. This resulted in a chopping interval on and off of 30 seconds each.

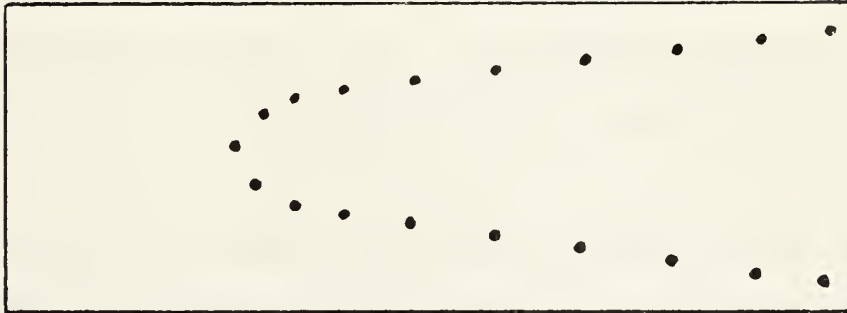


FIGURE 13A

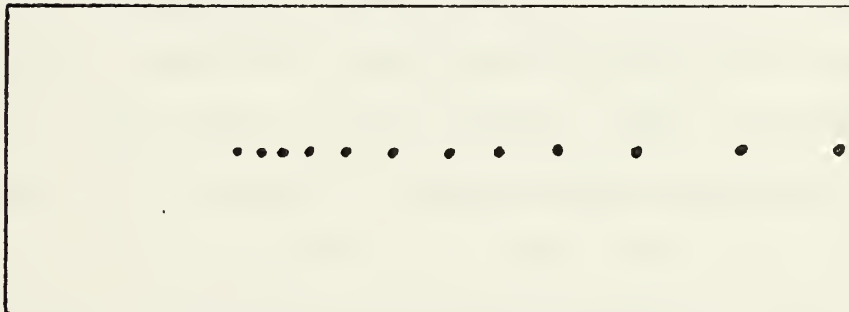


FIGURE 13B

MULTIPASS REFLECTIVE CELL
MIRROR REFLECTIONS

The signal from the detector was then put into a biasing circuit. This circuit was needed because on the lower scales of the voltmeter the zero reading from the detector caused fluctuations which were off scale. In this study, the setting used was 1 mV. This circuit enabled any background d.c. bias to be eliminated for more accurate readings.

The resulting signal from the biasing circuit was then fed into a microvolt meter, which would deflect an amount proportionate to the incoming light intensity. This allowed visual readings to be taken. The output of the meter was relayed into a strip chart recorder in order to obtain a permanent record. The alignment was all accomplished with a He-Ne laser. The next step was to use a CO₂ laser. Initially the output power of the laser was too great because of the power limitations of the detector. A collimator tube was used to both reduce the laser power through diffraction effects and to help align the CO₂ laser. With the He-Ne laser in place the collimator with an output aperture diameter of .5 mm was placed in the beam. The collimator position was then adjusted so that the output on the voltmeter was maximized. A second flat aperture of 4 mm was placed at the cavity input. Once these two had been properly aligned and the output maximized the He-Ne laser could then be removed. If the laser was later replaced and its position adjusted till a maximum output was again obtained, it was observed that the same number of reflections appeared on the

mirror as before. This fact was used in determining the overall path length of the CO_2 laser since it was assumed the CO_2 beam traveled the same distance as the He-Ne beam.

Again the He-Ne was removed and the CO_2 laser was put in its place. Its position was adjusted so that a maximum output was observed on the meter. Once this was accomplished care was taken to avoid touching the laser, collimator or cavity cell. The detector however could be moved slightly to maximize the output. Upon accomplishing this the next step was to introduce a sample into the cavity. With the sample in the cavity the maximum meter reading with and without the sample were used to determine the susceptibility. This procedure was repeated for both He-Ne and CO_2 .

In any measurement the flow of zinc oxide was not left on for an extensive period of time. This insured that a build up did not occur too quickly in the cavity. Also this prevented the zinc oxide particles from exceeding the protective ability of the air curtain and degrading the mirrors. One method of observing the mirror conditions was to observe the maximum meter readings after the sample had passed through the cavity. If the empty cavity readings returned to values approximately the same as those prior to sample introduction, then the mirrors were not seriously degraded.

By varying the flow rates of the hydrogen and oxygen the density of the particles and thereby the filling factor can be changed. The filling factor depends on P the ratio of the flow rate of hydrogen to the total flow rate of hydrogen plus nitrogen. In this study, assuming complete conversion of zinc vapor to zinc oxide

$$f = \frac{PM}{\rho RT} = \frac{C}{8+C} / \rho RT \quad 3.1$$

where C is the flow rate of hydrogen in cu. ft./hr., ρ is the density of zinc oxide ($\rho = 5.47$ gm./cc.), and T is the temperature °K.

2. Fabry-Perot Interferometer

Figure 14 is a block diagram of the Fabry-Perot apparatus. The oven and sample preparation are the same as previously described. Initially the measurements were attempted on a flat table but acoustic vibrations caused too much movement of the resonance peaks. A holographic table was obtained and used in subsequent measurements. The table consisted of a massive metal table approximately 200 pounds (24" x 44") sitting on four small rubber inner tubes. Because of the massive metal table the frequency response to acoustic and other noise vibrations in the laboratory was poor and the table remained stationary. Again the cavity was placed in a ventilating hood. This time the laser was mounted on an aluminum stand directly in front and about

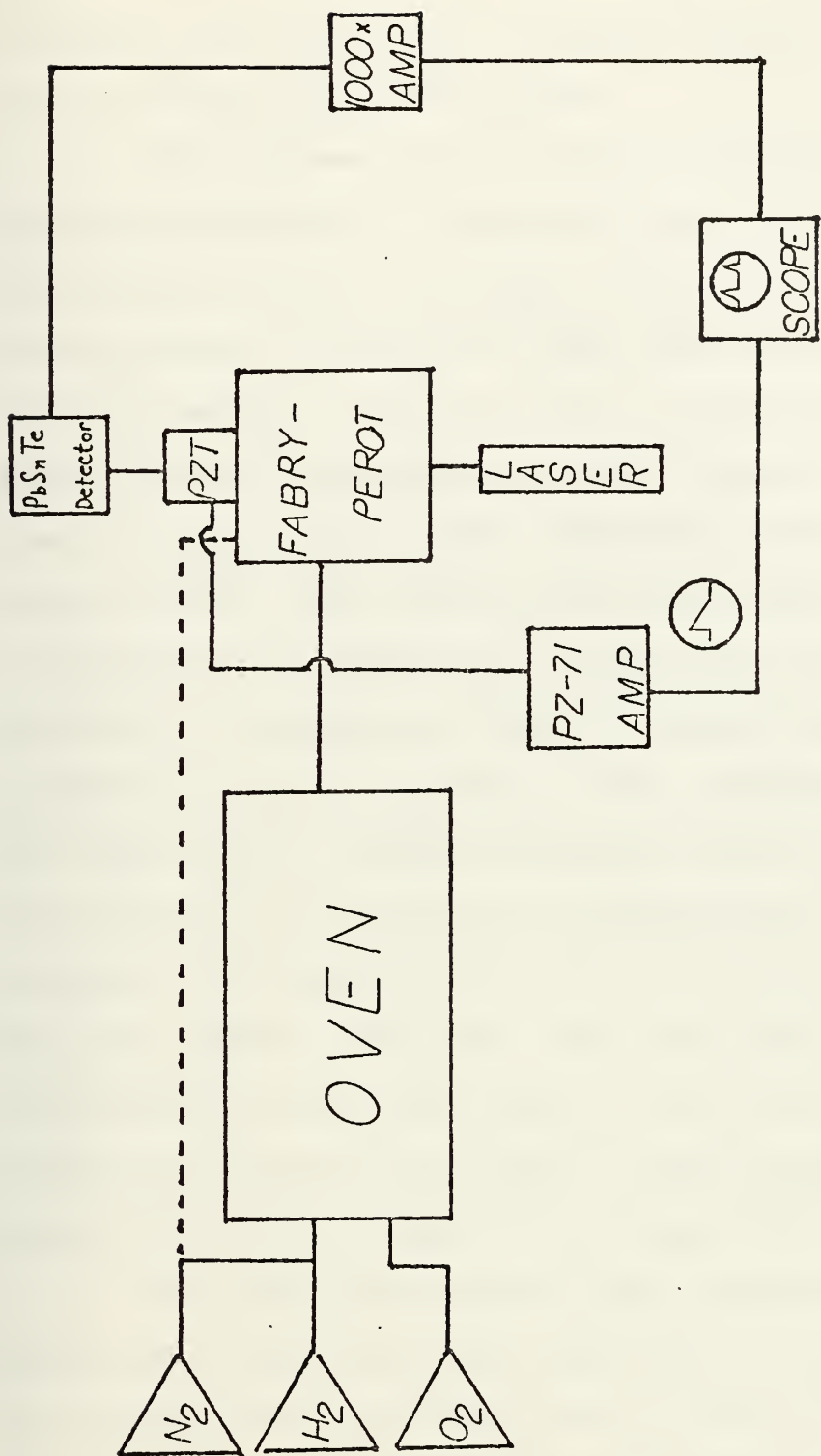


FIGURE 14
BLOCK DIAGRAM
FABRY-PEROT INTERFEROMETER

one meter away from the input to the Fabry-Perot interferometer. The aluminum stand was placed on foam pads and weighted with lead bricks to prevent acoustic vibrations from affecting the laser output.

The alignment of the Fabry-Perot interferometer proceeded as follows. The He-Ne laser beam was passed through the center of the input mirror to the Fabry-Perot interferometer. The tilt of the laser was adjusted so that the beam was also centered on the output mirror. A reflected beam from the input mirror was also observed on the laser face. By making the proper adjustment of the tilt of the mirror and the laser these three beams could be brought into a straight line. Doing this insured the incoming light was parallel to the optic axis of the interferometer. Upon completion of the first step a fine adjustment was made with the input mirror gimbled micrometer dials by observing that the pattern on the face of the output mirror was actually two dots. By adjusting the tilt of the input mirror these dots were made to coincide. The result was a set of circular interference rings which could be observed behind the output mirror with the aid of a piece of white cardboard. This however was not the final set of rings to be observed.

Once the first set of rings was obtained the subsequent adjustments were made with the output mirror. By carefully adjusting the mirror a second set of rings with much more contrast was brought into focus. This second set

was a result of focusing the return beam from the output mirror directly back on the incoming beam. Here the adjustments were very critical, a slight movement of the mirror tilt could completely defocus the rings. The final fine adjustments were made with the piezoelectric translator (pzt) amplifier controls. Because of the large size of the central bright fringe it was not necessary to filter out the higher order rings. The detector observed only the central fringe.

This central fringe was fed into a PbSnTe detector cooled with liquid nitrogen. The output was circuited through a 1000x amplifier to the vertical axis of an oscilloscope. The horizontal axis was triggered by the internal sawtooth wave generator of the oscilloscope. This internal sawtooth was set at 15 volts and was used to drive a Burleigh PZ-71 amplifier and Burleigh piezoelectric device. The purpose of the pzt was to axially scan the Fabry-Perot interferometer. The bias and gain controls on the PZ-71 amplifier could be adjusted so that the pzt would scan from 0 to 8 microns at a rate of up to 5 KHz. This scanning produced the Fabry-Perot resonant pattern discussed previously. It was observed that, once the rings had been set, vibrations did not permanently distort the resonance. For example if the table were bumped lightly the peaks would jump about but would return to the initial position in a short period of time (5-10 sec.). This greatly reduced any stringent requirements for vibration suppression in the laboratory.

It also enabled the detector to be resupplied with liquid nitrogen, which was required about every 35 min., without complete system realignment.

Once the initial alignment was made the CO₂ laser replaced the He-Ne laser in a manner similar to that previously discussed. A collimator was placed in the He-Ne beam and adjusted till maximum transmission was obtained. Instead of a second aperture a piece of white cardboard was placed so that it could be moved in and out of the beam. An "x" was marked where the He-Ne beam struck the cardboard. The He-Ne laser was then removed and the CO₂ laser replaced it.

The coarse adjustments for the CO₂ laser were as follows. A thin piece of white paper was placed directly in front of the collimator output. The laser was moved until the paper was observed to be charring. Because of the laser power this could be observed quite easily. The paper was then removed and one CO₂ Thermal Imaging Plate was placed in the beam just in front of the white cardboard with the "x". By illuminating the plate with a small ultra-violet source the beam could be seen as a dark spot on the yellow imaging plate. The CO₂ laser was moved so that the dot and the "x" coincided. This technique was coarsely done by eye. The plate and cardboard were then removed and the fine adjustments on the finesse were made with the mirror gimble micrometers and the adjustment dials on the PZ-71 amplifier. This was accomplished by maximizing the resonance peaks on

the scope. Although the above description seems extremely coarse it worked surprisingly well. The entire apparatus could be aligned in most cases in less than 30 min. This proved extremely useful should the beam be moved or a piece of equipment need replacing; it could be done and the apparatus could be back in running order in a short period of time.

Once the laser and interferometer were aligned, measurements were ready to be taken. The sample was delivered to the interferometer cell the same way as previously described. Upon entering the cavity the predicted shift (Fig. 10) was observed, as seen in Fig. 25. This figure shows only one of the resonance peaks of Fig. 10. A polaroid, double exposure picture was taken; one picture being taken before the sample entered the cavity and the second with the sample in the cavity.

Two electrical plates, 4.5 cm. by 13.4 cm. and .1 cm. thick were placed 1.5 cm. apart above and below the beam distribution in the cavity. This allowed an electric field to be applied to the sample while the measurements were being taken. Since the laser was vertically polarized, the application of an electrical field aligned more particles along the direction of polarization.

Because the high finesse of the cavity required a detector which had a short time constant, lead-tin-telluride was used rather than the thermopile. Since the characteristic

wavelength of the detector was 8 to 12μ and since the mirror coatings were specifically ordered for 10.6μ radiation, the Fabry-Perot measurements were taken only with the CO_2 laser and not the He-Ne laser. A word of safety should be added here. Because of the power levels produced by the CO_2 laser, no one was allowed in the laboratory without either 1) standard reading glasses, since glass is a poor transmitter of 10.6μ radiation; or, 2) specially designed IR glasses.

C. CAVITY DESIGNS

1. Initial Multipass Reflective Cell

The initial design for the reflective cell consisted of a rectangular box $13" \times 8 \frac{1}{2}" \times 4 \frac{7}{8}"$ high, made of $\frac{1}{4}"$ and $\frac{1}{8}"$ plexiglass. The $\frac{1}{4}"$ was used for top and bottom and the $\frac{1}{8}"$ for the sides. Three runners, $13" \times \frac{1}{2}" \times \frac{1}{4}"$, were placed along the bottom for support and to enable the mirror mount to be easily inserted. To the front of the box was attached a rectangular aluminum funnel, $6 \frac{1}{2}"$ long. The smaller end of the funnel was shaped into a circular aperture, $1 \frac{15}{16}"$, which fit over the output tube of the furnace. The purpose of the funnel was to aid in dispersing the zinc oxide throughout the cell. In one side of the box a $1"$ beam input hole was cut and diagonally across the box a $1"$ output hole was cut.

The mirror mounts were placed inside this cavity. These consisted of a piece of $\frac{1}{2}"$ aluminum, $11" \times 8"$. On

each side of the mount two aluminum strips, $1/4"$ x $1/2"$, were fastened so that the mirrors could be placed between them and tightened with screws. The mirrors themselves were $1/8"$ x 3" x 9" aluminum coated plate glass. One mirror was fixed in place and the second could move laterally to the long axis of the first by means of a threaded knob. The above description is pictured in Fig. 15.

The initial idea was to have the beam reflected as in Fig. 3. The purpose of the movable mirror was that as more and more length of mirror was used, a greater number of dots could be observed on the mirrors. It was hoped that as the mirror was moved the output dots could be counted to get a total path length.

The initial setup was made but it was quickly discovered that this method was too unstable. Unless the mirrors were exactly vertical with respect to each other, the reflections would not stay on the mirror. Since no adjustment in this dimension was possible, a new method had to be devised. It was also discovered that by tilting one mirror with respect to the other around a vertical axis, the reflections did not go all the way down the mirror but went a certain distance then returned to the initial input area. It was decided to incorporate this idea into the next design.

The next modification to the cell was to remount one of the mirrors. A piece of 90 degree angled aluminum was glued to the back of one of the mirrors and a slot

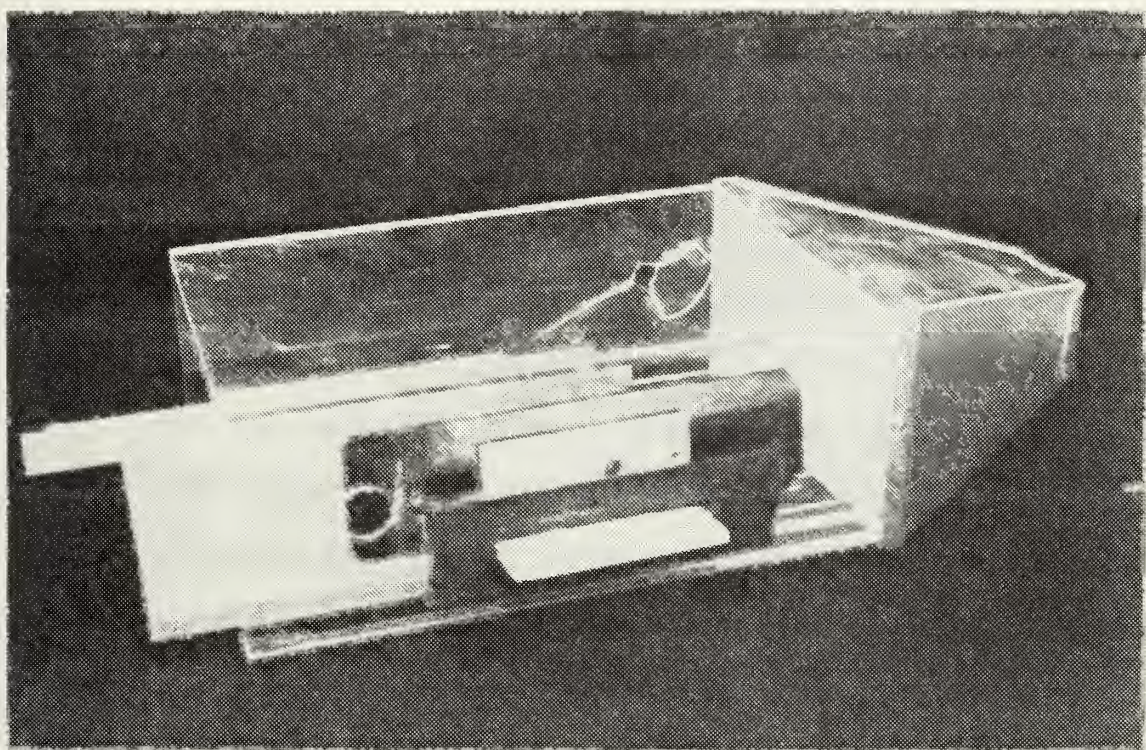


FIGURE 15
INITIAL MULTIPASS CELL

1/2" x 4 1/2" was cut on one side of the plexiglass box so that when the mirror was inside the box the other end of the angled aluminum protruded through the box. This protruding end was fastened via machine screws to a gimble mount giving the desired two degrees of freedom .

The entire apparatus was assembled using any necessary stands to insure height compatibility of all components. By adjusting the vertical tilt, the reflections could be kept on the mirror; and by adjusting the horizontal tilt the desired number of reflections and thereby the path length could be controlled. The last reflection from the mirror exited the back open end of the plexiglass box and was focused via a 10 cm. focal length lens onto a P.I.N. diode detector. The diode was encased in an aluminum tube approximately 2" long, painted black to reduce excess input of light. An 1800 Ω resistor was placed across the diode terminals and this voltage was fed to a micro-voltmeter. With the apparatus set up this way, the mirrors were aligned and a sample of zinc oxide was placed in the box. Data was taken but several disadvantages were noted: 1) After several minutes of "run time," the mirrors became coated and further readings became impossible. 2) Because of the volume of the box ($\approx .3$ cu./ft.) a great deal of time was required to fill and empty the box. 3) The method of detection was applicable only to the He-Ne laser since the lens would not pass 10.6 μ radiation, and the detector wavelength limit was $\approx 1\mu$. The subsequent

design described next attempted to correct these deficiencies while improving some of the discovered highlights of this system.

2. Final Multipass Cell

The most pressing problem which had to be solved was to protect the mirror from zinc oxide coating. At first common saran wrap was placed around the mirrors for protection but it was quickly discarded when it was discovered that the wrap dispersed the beam and would remove the aluminum coating from the mirror wherever it touched the mirror. An air curtain was decided upon. This was accomplished by building a "box on top of a box." This upper box was airtight except for two slits cut in the bottom, just in front of the mirrors and a gas inlet port. By feeding the upper box with nitrogen, an air curtain was created to protect the mirrors. This air was vented through slots cut in the bottom of the apparatus.

This final box was built much smaller than the first being only 7" x 7 1/2" x 2 1/4" high. Again a 2" funnel was used to connect the cell to the oven output. The mirrors were made from 1/8" plate glass, one being 1" x 5 1/2", and the second was 1" x 5 3/4". The difference in length was to allow the beam to enter the cell. The box was designed so that the top 1/4" was sealed and fitted with a hose connector, 1/8" pipe thread to 1/4" hose, so that nitrogen could be pumped in. Initially, the air curtains used were a series of small holes (# 55 drill) drilled 1/8 inch apart along the bottom of the upper box, in front of the mirrors.

When the apparatus was assembled and a particulate suspension introduced, the curtains proved ineffective in keeping the mirrors clean. It was then decided to modify this design to increase the efficiency of the curtains. Seven-eighths of an inch in from each side of the box, a 1/16" wide slit was cut in the upper portion to serve as the air curtains. Directly below these on the bottom plate of the box were cut two slits 6" x 1/2" to act as exit ports for the sample. The back end was covered with thin cardboard with a space cut out to allow the exit beam passage. The purpose of the cardboard was to reduce the effects of drafts, in the hood, on the sample.

The longer mirror was glued to a 1/4" piece of aluminum the same size as the mirror which was then mounted via machine screws directly to one side of the plexiglass box. The second mirror was mounted similarly to that previously described with a 90° piece of aluminum. A 1/4" diameter hole was cut in the side of the plexiglass to allow the beam to enter. The output mirror was a 1" square aluminum coated glass mirror placed at the end of the box opposite the funnel. It was positioned so that it intercepted the final reflection of the beam. The above description is depicted in Fig. 16a, b.

The box alignment was the same as previously described. The vertical tilt was adjusted to allow the beam to directly fall back on itself as in Fig. 13b. The horizontal tilt was adjusted to get the desired path length.

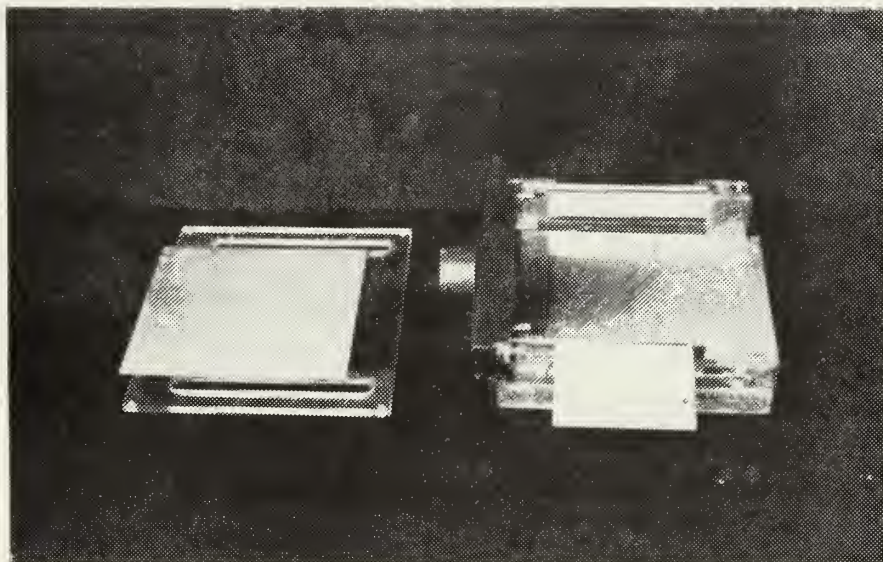
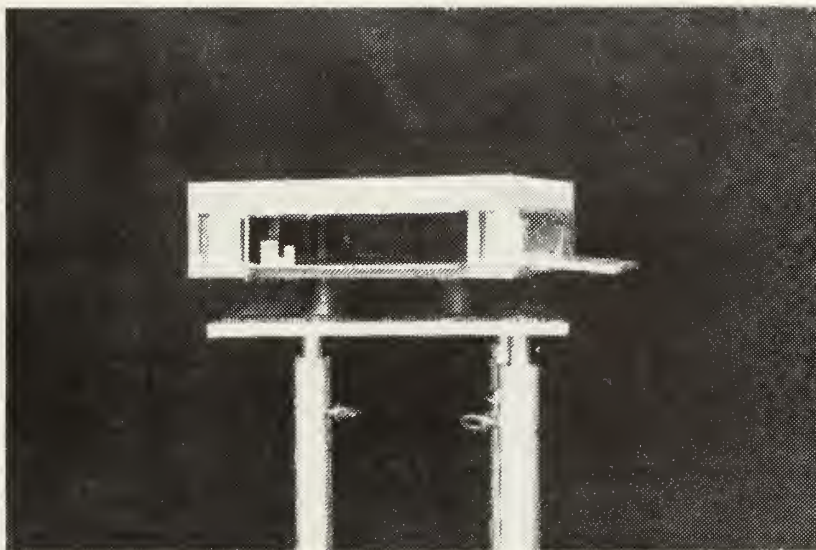
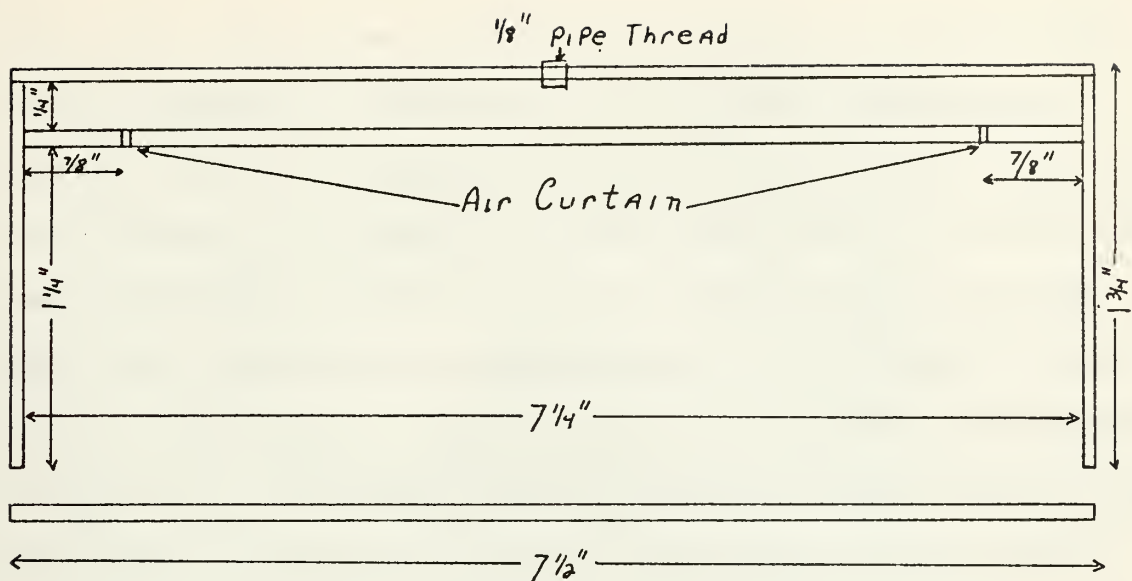
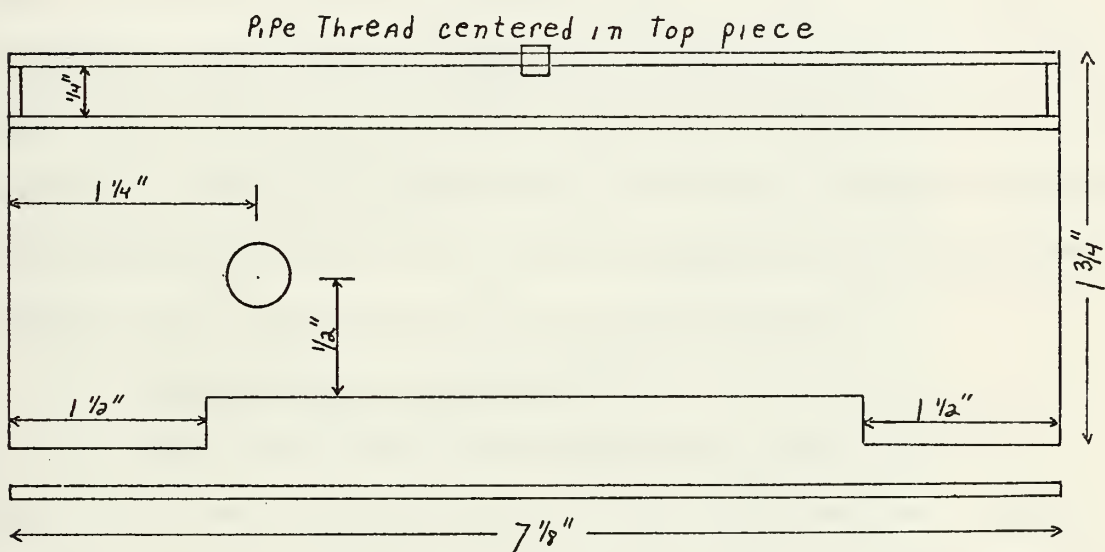


FIGURE 16A
FINAL MULTIPASS REFLECTIVE CELL



REAR VIEW



SIDE VIEW

FIGURE 16B
FINAL MULTIPASS REFLECTIVE CELL

The final reflection was directed through the rear of the cavity and onto a detector. In this case a spherical mirror was used to focus the beam on the detector. The lens was changed to a mirror to enable the system to be used for both the He-Ne and the CO₂ beams without having to worry about the transmission characteristics of the lens at each of the wavelengths. The detector now used was a thermopile encased in a 2 in. long aluminum tube to reduce stray light. The output leads were shielded from stray radiation and circuited via shielded cables to a micro-volt meter.

Data was then taken and the system proved very good. The alignment process required about 30 min. and it was found that the mirrors required cleaning only every other day. This was easily accomplished by washing carefully with acetone. Except for one mirror which was dropped and broken the system used the same mirrors throughout the experiment showing the practicality of the air curtains.

3. Fabry-Perot Interferometer

The Fabry-Perot interferometer consisted of two parts as shown in Fig. 17a, b. The first was an aluminum holder for the mirrors and the second was a plexiglass box to hold the sample and protect the mirrors. The aluminum holder consisted of a 1/2 in. piece of aluminum 15 1/2 in. by 6 in. On this were mounted two gimble mounts separated a distance of twenty cm. One mount was fitted with a threaded ring to hold a one inch mirror in place. The second

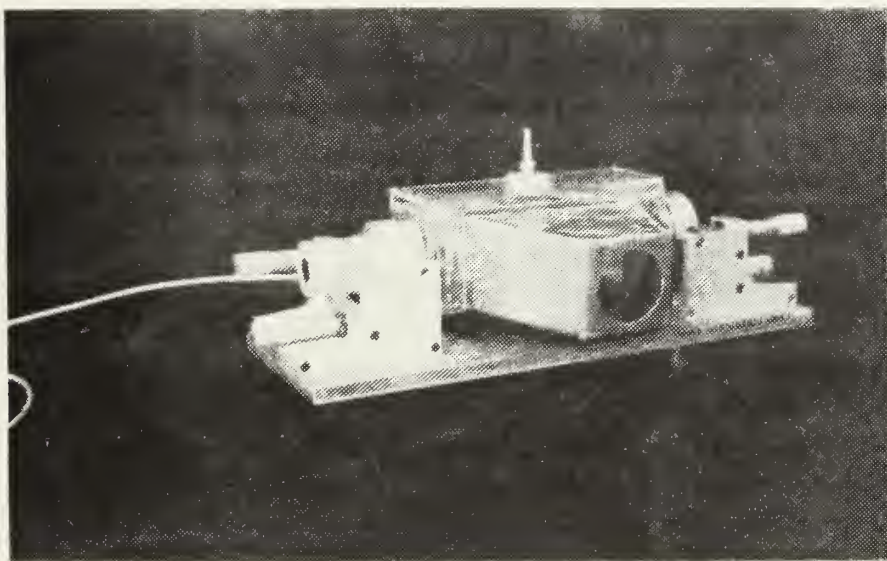
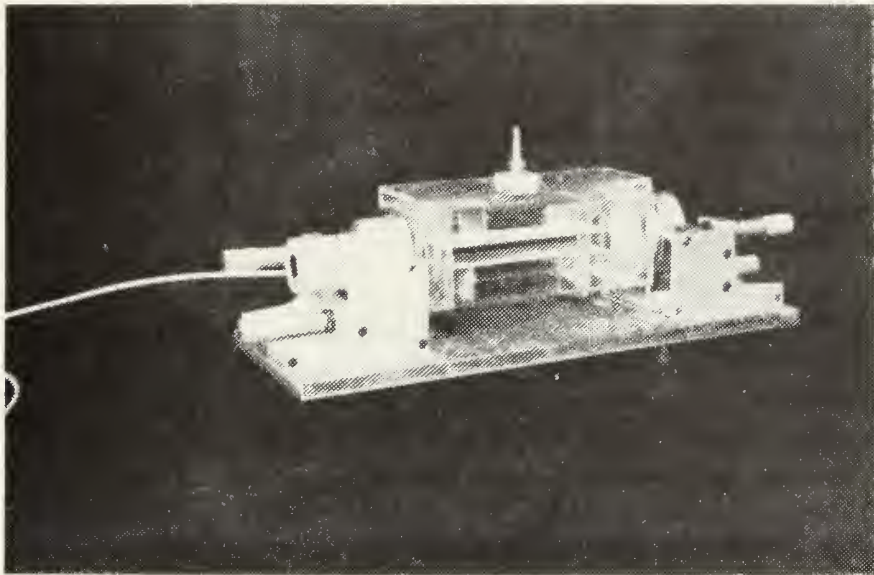
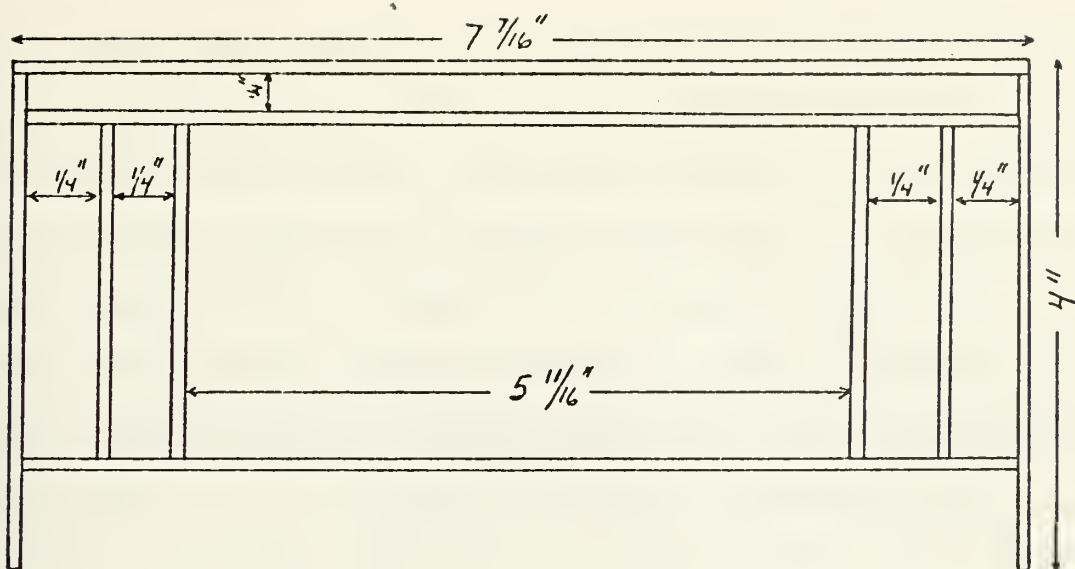
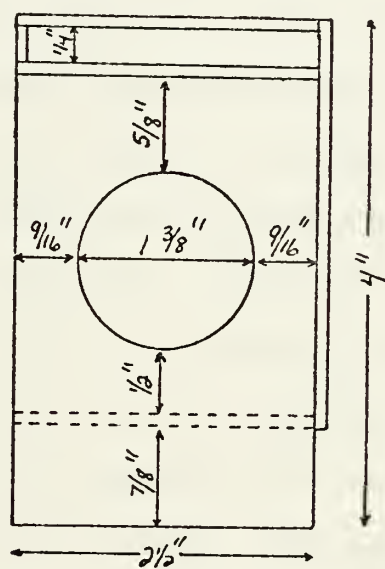


FIGURE 17A
FABRY-PEROT INTERFEROMETER



FRONT VIEW



SIDE VIEW

FIGURE 17B
FABRY-PEROT INTERFEROMETER

was fitted with a small tube about $1\frac{1}{2}$ in. in diameter which allowed the pzt device to be inserted and held tight. The mirrors used in this experiment were two 1 in. diameter zinc selenide substrate circular reflectors. One side was plane and the other curved with a radius of curvature of 20 cm. The curved side was coated for 98% reflectance at 10.6μ . The guaranteed surface smoothness was a minimum of $\lambda/100$ over .6 in. Because of the high tolerances the mirrors were costly and had to be handled with extreme care. When mounted, one in the aluminum mount and one in the pzt device, the mirrors were separated by a distance of 20 cm.

A plexiglass sample cell was placed between these mirrors. It was made of $\frac{1}{8}$ in. plexiglass $7\frac{1}{2} \times 2\frac{3}{4}$ in. $\times 4$ in. high. Again the device made use of a built in airtight section to provide the air curtain. Because of the mirror cost it was determined two air curtains should be utilized for extra protection. This was accomplished by cutting two slits $1\frac{1}{2}$ in. $\times \frac{1}{32}$ in. in the bottom of the airtight portion. Each slit was separated by a plexiglass baffle with a $1\frac{3}{8}$ in. diameter hole cut in the baffle to allow the light to pass through. The same size hole was cut in the sides of the box for light passage. The back of the sample cell was covered with a piece of plexiglass with a slit $\frac{1}{4} \times 3\frac{1}{2}$ in. cut to act as an exit port. The above description is depicted in Fig. 17a, b. A $4\frac{1}{2}$ in. copper funnel fit on the front of the box to allow the sample to enter.

The plexiglass cell fit between the mirrors of the Fabry-Perot interferometer. With the box in place and the laser aligned fluctuations of the resonance peaks due to thermal variations were greatly reduced. From Eq. 2.32 $\nu = qc/2\eta\ell$. Now a desired temperature dependence is to be found. If a change in temperature causes a change in the lineshape, $d\nu$, then this change is given by

$$d\nu = - \frac{qc}{2\ell\eta^2} d\eta \quad 3.2$$

where $d\eta$ is the difference in refractive index of the material between the mirrors due to a difference in temperature. This change relative to the distance between the peaks $\Delta\nu$ is

$$\frac{d\nu}{\Delta\nu} = \frac{-qc}{2\ell\eta^2} \frac{2\eta\ell}{c} d\eta = - \frac{q}{\eta} d\eta = - \frac{2\ell}{\lambda} d\eta \quad 3.3$$

The index of refraction can be written as

$$\eta = 1 + .0002929 \frac{\rho}{\rho_0}$$

where ρ is the density of the material and ρ_0 is the density of air. Remembering $\rho = PM/RT$ this reduces to

$$\eta = 1 + .0002929 \frac{T_0}{T} \quad 3.4$$

and

$$d\eta = - .0002929 \frac{T_0}{T^2} dT \quad 3.5$$

When $\frac{dv}{\Delta v} = \frac{1}{F}$, then dv is a one linewidth change, and assuming the initial temperature of the sample is that of the air $T_0 \approx T$, then by substituting Eq. 3.5 into 3.3

$$dT = \frac{\lambda T_0}{2\ell F(.0002929)} \quad 3.6$$

where dT is the temperature change required for a one linewidth change. For a cavity finesse of say 50, $dT = .5$ °C. The plexiglass box between the mirrors reduces air currents and helped reduce this temperature fluctuation.

When assembled the entire unit was placed on the holographic table and measurements of the cavity finesse were taken. The ventilating hood was turned off during the actual data taking but was turned back on immediately afterwards. The reason for this was that the motor for the hood caused vibrations and strong air currents resulting in fluctuations of the resonance peaks.

D. SUPPORTING EQUIPMENT

1. Micro-Volt Meter

This was used with the multipass reflective cells. It was an HP-419A DC Null Voltmeter with a capability as low as 1 μ volt. Because of fluctuations in the zero reading it was not used below 30 μ v. It also provided a 0-10 volt variable output which was fed to a Honeywell x-y recorder.

2. Oscilloscope

This was a Tektronix Type 545A oscilloscope. The scope had an internal sawtooth wave generator which was used to run the pzt device. This sawtooth was fed to a voltage divider which gave a variable output from 0-20 volts. The frequency of the sawtooth was controlled by the horizontal sweep of the scope.

3. Pzt Translating Circuit

This consisted of a Burleigh Model PZ-71 amplifier and a Burleight Model Pz-80 Translator/Aligner as shown in Fig. 18. The PZ-71 was a high voltage DC Operational amplifier which was divided into three sections: 1) the high voltage DC OP Amp, 2) Tilt trim control — this insured there was no angular deflection in the mirror as it scanned, and 3) The alignment bias — this enabled fine adjustments in the mirror alignment to be made electronically. The amplifier had a 0-100 gain with a continuously adjustable bias from 0-1000 v. The input to the device was clipped at ± 30 volts DC with respect to ground. The input to the amplifier was the sawtooth described above and the output was fed to the translator.

The translating device was used to piezoelectrically position a 1 in. mirror both axially and angularly. The device had a cup with a threaded ring capable of holding a 1 in. mirror, which translated at $8 \mu\text{m}/1000 \text{ v.}$ The output was a .6 in. clear aperture. The device consisted of

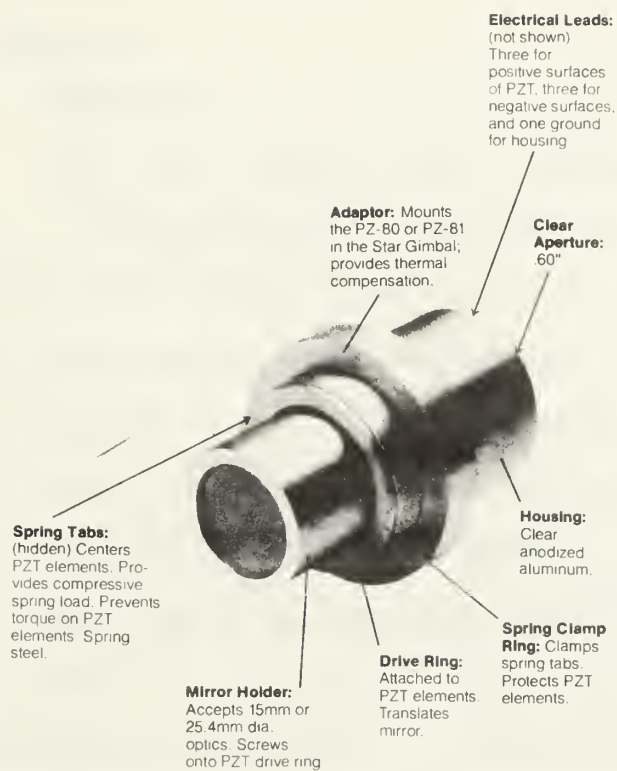


FIGURE 18

PIEZOELECTRIC TRANSLATOR

three piezoelectric elements set 120° apart, each of which could be independently controlled. This allowed translation and angular positioning of the optical element.

4. Detectors

a. Thermopile

This was a SENSORS Inc. Type S-15 thermophile detector. It consisted of 28 junctions with an active area of $2.25 \times 10^{-2} \text{ cm}^2$ (1.5 mm x 1.5 mm). The model used had a CaF_2 window which required storage in a moisture free container when not in use. The responsivity was 8-12 volts/watt with a time constant of 20-40 milliseconds.

b. Lead-Tin-Telluride (PbSnTe)

This was a photovoltaic detector with a sensitive area of $30 \times 10^{-4} \text{ cm}^2$ made by Raytheon Inc. It had a barium flouride window and operated in a wavelength range of 8-12 μ . Its operating temperature was 77 °K which required a liquid nitrogen coolant supply. The detector had its own dewar for this purpose. The maximum allowable safe input power was 200 mW.

5. Collimator

This consisted of an aluminum tube 1/8 in. thick, with a 1 1/4 in. inner diameter and 5 3/4 in. long as shown in Fig. 19. One end was open and the other threaded to accept a cap with a 1 mm. hole in the center. The entire inside was painted black to dissipate the unused laser light. The whole system was then mounted on a gimble mount which

allowed vertical and horizontal translation. The purpose of the collimator in addition to helping align the beam was to reduce the power through diffraction. Since the laser beam was 4.5 mm. in diameter a large portion of the beam is reflected back into the collimator. Using the standard diffraction results the angular diffraction of a CO₂ beam after passing through the 1 mm. aperture is

$$\sin \theta \approx \theta = 1.22 \lambda/d \quad 3.7$$

with a resulting Airy diffraction pattern. If it is assumed that all the power is in the central lobe, then at a distance x the power density is reduced to

$$P = P_o [A_a/A] \quad 3.8$$

where A_a is the area of the 1 mm. aperture, A is the area of the central diffraction lobe ($A = \pi(x\theta)^2$, θ in radians), and P_o is the power density of the laser.

Since CO₂ radiation produces corneal rather than retinal damage Myers in Ref. 14 lists the maximum permissible exposure (MPE) as 200 mW/cm². Using an extra safety factor of 1/2, with the above collimator a distance of about one meter was considered to be safe, however no chances were taken and eyeglasses were still required in the laboratory.

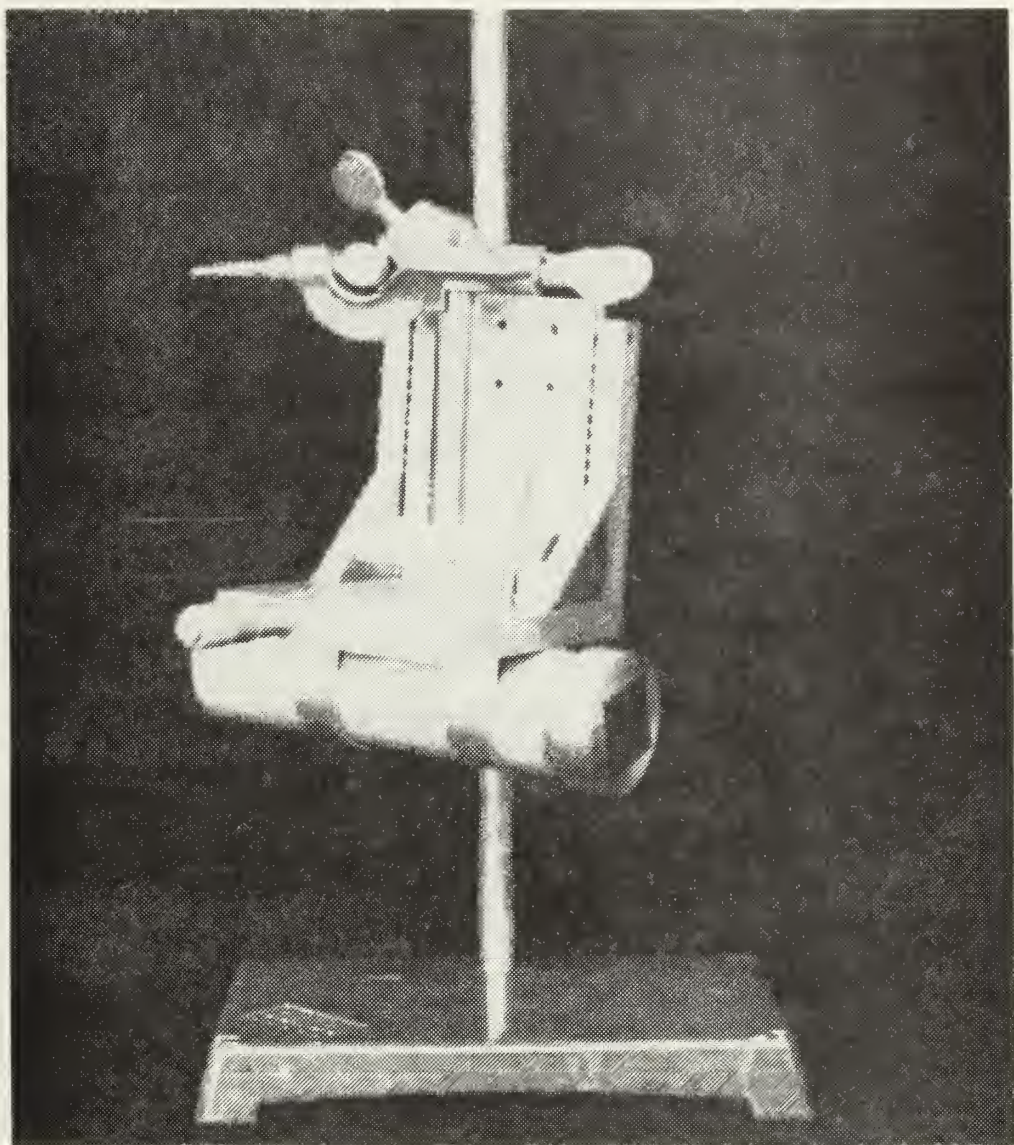


FIGURE 19

CO₂ LASER COLLIMATOR

6. He-Ne Laser

A CW Radiation Inc. Model LS-1 He-Ne laser was used in this study. It produced 1.8 mW of vertically polarized radiation at 6328 \AA . It was used strictly for the multipass cells and just to align the Fabry-Perot interferometer because of frequency instabilities and the tendency to resonate in several longitudinal modes. Because of the constant shift from one mode to another it was rendered impractical for use with the Fabry-Perot interferometer. In the multipass cell intensity not frequency stability was necessary and this laser could then be used.

7. CO₂ Laser

A Sylvania Model 941 CO₂ laser was utilized. It produced 3 watts of continuous power with vertical polarization at 10.6μ , and a frequency stability of one part in 10^9 . This enabled a single resonant peak to be observed with small probability of shift during the measurement cycle. The laser itself was water cooled and the output power could be varied slightly via an adjustment on the laser tube current. It must be noted however that the manufacturers recommended warm up time be observed. During this period frequency shifts were quite prevalent rendering data acquisition impossible.

IV. RESULTS

Section III gave a basic description of the proposed method of measurement, some modifications necessary to produce better results, and predicted results that should be observed. This section will justify the feasibility of the proposed method and further elaborate on slight modifications which were deemed necessary after the apparatus had been assembled. The initial measurements were taken in the multipass reflective cell and upon completion the Fabry-Perot interferometer was assembled and subsequent measurements were taken with this system. Results with the two systems will be discussed separately below.

A. MULTIPASS REFLECTIVE CELL

The multipass reflective cell of Fig. 15 was used in the first experiments. Initially a strip chart recorder was not used. Maximum voltmeter readings with and without the sample were recorded. This system had some inherent disabilities which rendered it impractical for use, as are indicated below. In order to overcome these difficulties a second cell was designed, Fig. 16, which proved highly more satisfactory and made the system practical for future use.

1. Problems Encountered

Several major problems were encountered in the initial cell design. Approximately 4-5 minutes were required to fill and to empty the cell of sample each time a reading was to

be taken, which was excessive. With this amount of time with the sample present in the cell the probability of the mirrors becoming coated was too great.

After several minutes of "run time" the mirrors became coated and had to be removed and cleaned, necessitating realignment of the system. This was observed by noting the maximum meter reading before introduction of the sample and after it was cleared. It was observed that these two readings varied excessively indicating mirror degradation. It was felt that a system requiring disassembly this frequently was of little use in any measurement process.

In taking the readings the maximum meter reading fluctuated slightly during the measurement cycle. This made any accurate results difficult to obtain. Also with an unchopped input beam the output had long term (3-5 min.) time variations, necessitating using an average value for both the clear cell and the cell with the sample.

The design of the next cell attempted to correct these difficulties. First a strip chart recorder was installed using the output from the voltmeter which enabled a permanent and more accurate result to be obtained. A chopper as previously described was incorporated at the input to compensate for time variations or drifts by continually recalibrating the zero level. A new cell was made whose dimensions were much smaller. This reduced the filling and emptying time so that now it required about 30-40 sec.

to fill and empty the cell. This new cell also incorporated the air curtain as previously discussed. Initially the holes drilled 1/8 in. apart were used but these proved ineffective in keeping the mirror clean. It was decided to go to the slit design discussed in Section III, which proved very successful.

2. Preliminary Zinc Oxide Results

In an attempt to prove the feasibility of this system zinc oxide was used as a measurement sample. Figure 20 is an example from the unchopped beam using a P.I.N. diode detector. With the chopper installed and using a thermopile detector Fig. 21 is the result. The time scale (horizontal axis) is set at 5 min./in. From this figure readings of I_0 and I could then be taken. Also by counting the number of reflections the total distance the beam traveled could be determined. Knowing these values σ_c/V could be determined from Eq. 2.17 with the help of Eq. 3.1.

From Fig. 21 it can be seen that the empty cell reading would return to its initial value after sample purging indicating the air curtains were operating correctly. A second method could be employed for observing the effect of the sample on the mirrors. By looking directly down on the top of the cell, with a sample present, the path of the He-Ne light beam could be observed. Without the air curtains on, the beam was observed all the way up to the mirrors. With the air curtains on the beam was observed to stop at the

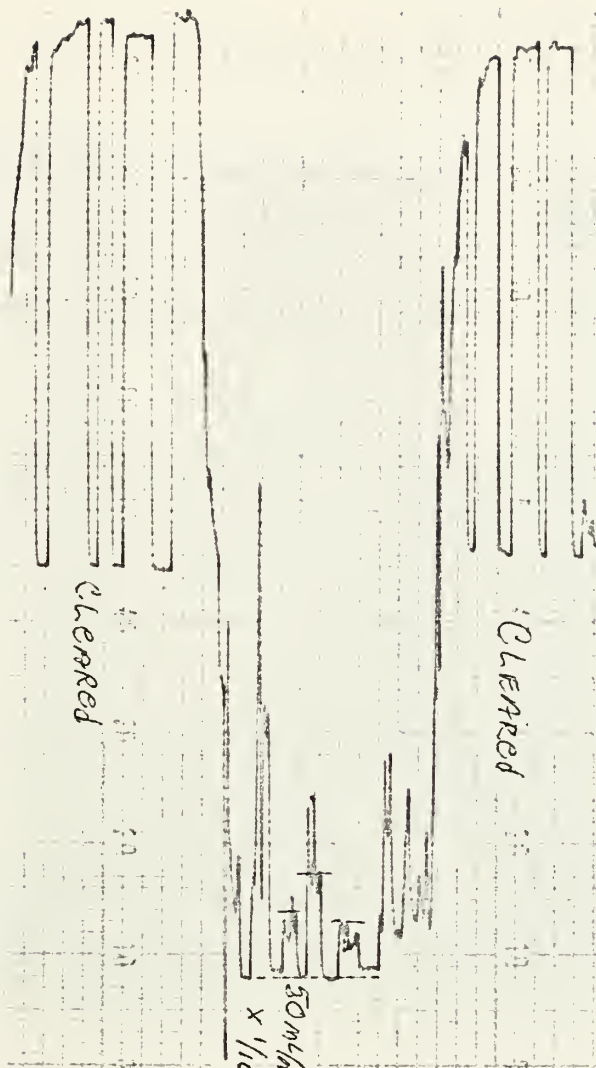


FIGURE 20

UNCHOPPED MULTIPASS REFLECTIVE CELL OUTPUT

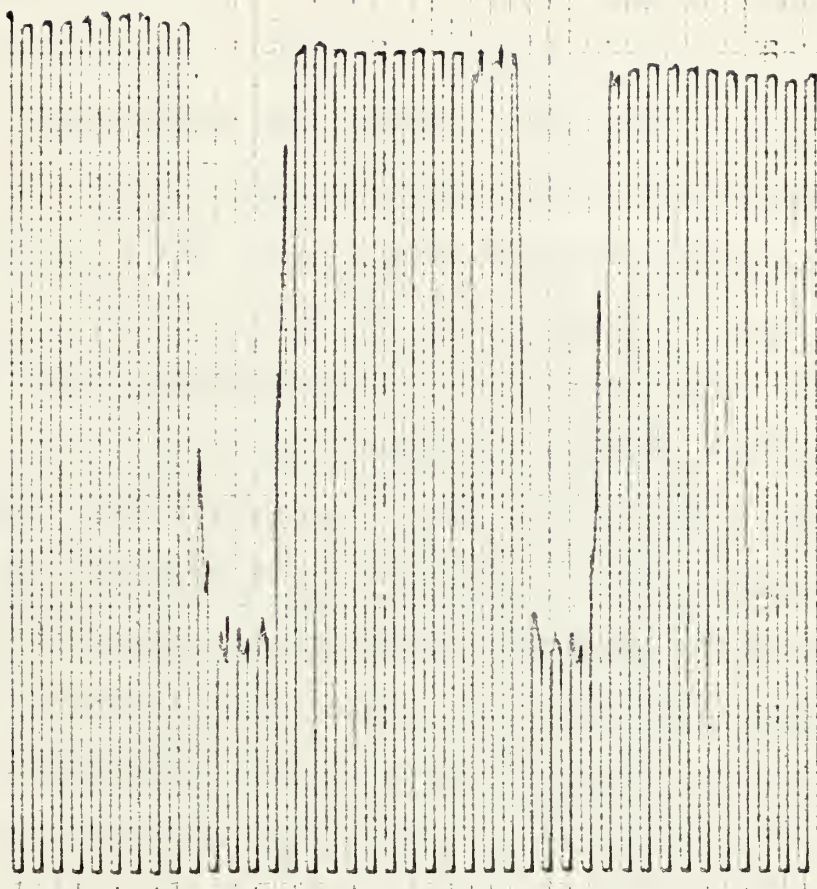


FIGURE 21

He-Ne

CHOPPED MULTIPASS REFLECTIVE CELL OUTPUT

position of the curtains. This enabled a quick visual check of the mirrors to be made. Figure 22 is an example of the output of a CO₂ laser using a chopper and collimator previously described. The different sample heights correspond to different filling factors.

One problem was noticed. Because of the velocity of the air rushing past the mirrors (≈ 16 cm./sec.) turbulence was created in the cell. This could be observed both in looking in the cell with the He-Ne beam on and a sample present, and from the output data. From those portions of Fig. 21 and 22 when the sample was present, a variation in the output from a constant value can be seen. This variation is due to localized density changes in the path of the beam due to turbulence. By taking the average of the maximum and minimum values at each point a more accurate result for I could be obtained. It was observed that if the air flow to the curtains was reduced these fluctuations in the readings were reduced, but the mirror protection was also reduced. After several attempts it was decided that a flow rate of 8 cu.ft./hr. to the air curtains was sufficient to keep the mirrors clean and yet not have the turbulent effects be predominant.

The ease with which the system could be changed from He-Ne to CO₂ and vice versa shows the ability of this system to be used with any number of different wavelengths. One visible wavelength laser source is necessary however to aid

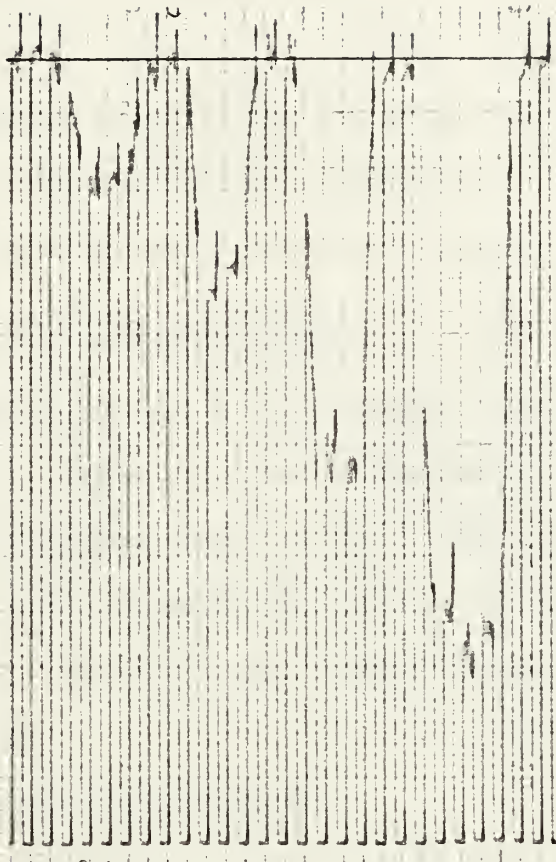


FIGURE 22

CO₂

CHOPPED MULTIPASS REFLECTIVE CELL OUTPUT

in the alignment process. Once aligned and the collimator in place a laser of any wavelength can then be used for measurements. Also laser power requirements are not a critical factor. In this study a 1.8 mW and a 3 W laser source were used. Since both power levels worked well it is conceivable a laser with any power between these two levels will work equally well, the only restriction being that an appropriate detector be employed.

B. FABRY-PEROT INTERFEROMETER

Upon completion of the multipass reflective cell experiment the apparatus was disassembled and the Fabry-Perot interferometer was set up. The purpose of this system, as stated previously, was to develop a method for measuring both the real and imaginary parts of the susceptibility.

1. Problems Encountered

When the Fabry-Perot system was initially assembled the most critical problem was movement of the resonant peaks due to acoustical vibrations. The apparatus was assembled on a wooden table and any stray vibrations resulted in peak movements which made accurate measurements impossible. Since the initial assembly did not have the plexiglass cell between the mirrors thermal variations due to drafts also added to the peak movements. Use of the ventilating hood caused great variations in the position of the peaks making readings impossible.

Since the direction of the laser was so critical to the position of the output rings and the CO₂ beam was invisible, a method of getting the CO₂ beam onto the center of the Fabry-Perot mirror was needed. Also the detector was cooled with liquid nitrogen and any system design had to encompass a method of easy access to the detector without disturbing any other system equipment.

The modifications made attempted to correct the above deficiencies. A holographic table was employed to reduce acoustical vibrations. With the plexiglass cell in place thermal variations were greatly reduced. These two modifications resulted in a stable resonance peak from which measurements could be taken. The CO₂ Thermal Imaging Plates were used to aid in placing the beam on the Fabry-Perot mirror. The ventilating hood was not used during the measurement cycle but only upon its completion to aid in clearing the cell. The holographic table proved stable enough so that even if it were bumped slightly while the detector was being filled, the resonance peaks remained the same.

2. Preliminary Zinc Oxide Results

Figure 23 is an example of the resonance peaks of the Fabry-Perot interferometer, corresponding to a finesse of 90. Through continued use this value was slightly degraded, due to the air curtains not being 100% effective, but still remained at a usable value of about 30-50. By

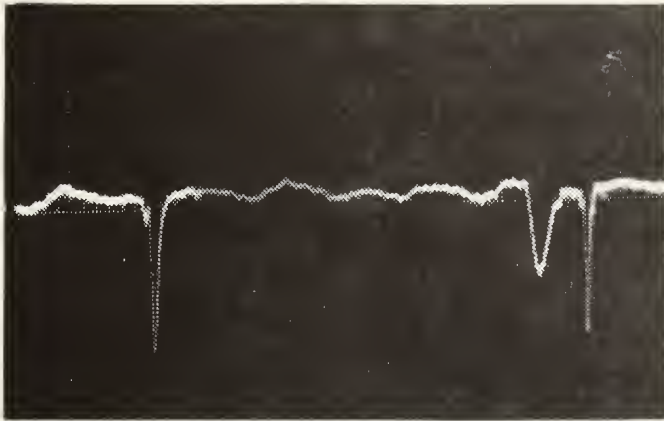


FIGURE 23
FABRY-PEROT FINESSE

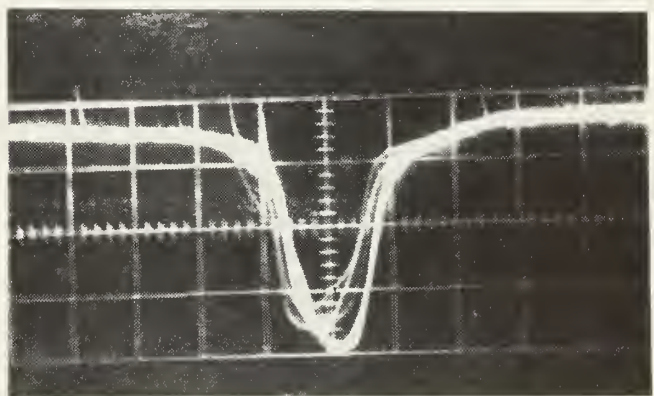


FIGURE 24
FABRY-PEROT
CAVITY STABILITY

expanding the scale and focusing on a single peak measurements could be taken. The stability of the resonance peak is shown in Fig. 24, which is five exposures taken 30 seconds apart without any sample. Since each measurement required only about 30 seconds little error is encountered as a result of drift during the measurement cycle. Several items could be the cause of these instabilities. The laser was water cooled and vibrations caused by the running water can cause slight cavity length changes which will cause frequency shifts. Also since a temperature change T_2/T_0 on the order of .5 °C can cause a one linewidth change, smaller temperature changes caused by drafts in the laboratory could easily cause observable shifts. A last item that could cause vibrations is acoustical noise. The holographic table is not perfect and some stray acoustical vibrations can be transferred to the Fabry-Perot interferometer resulting in slight frequency shifts.

One peculiarity was observed. By changing the flow rate of the hydrogen gas the direction of the frequency shift could be changed as shown in Fig. 25 a,b. Figure 25a corresponds to a flow rate of .48 cu.ft./hr. for hydrogen and .2 cu.ft./hr. for oxygen and a cavity finesse of 31. Figure 25b corresponds to a flow rate of .6 cu.ft./hr. for hydrogen and .15 cu.ft./hr. for oxygen. It is believed that this difference is due to the amount of water vapor produced in the reaction, since H_2 and O_2 are present in

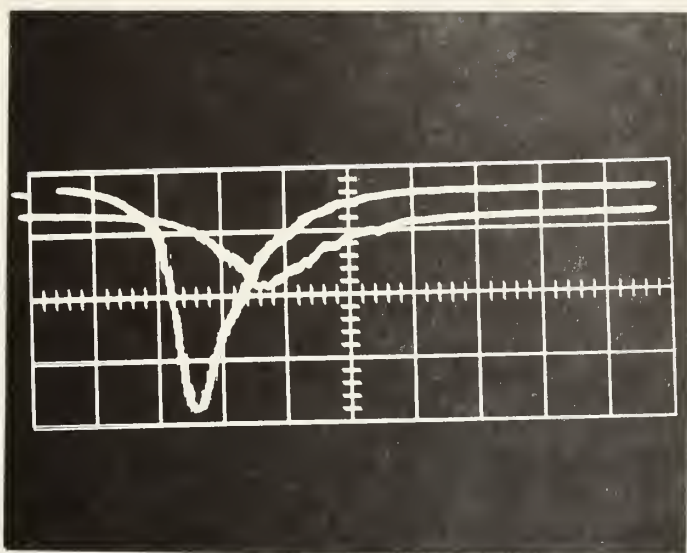


FIGURE 25A

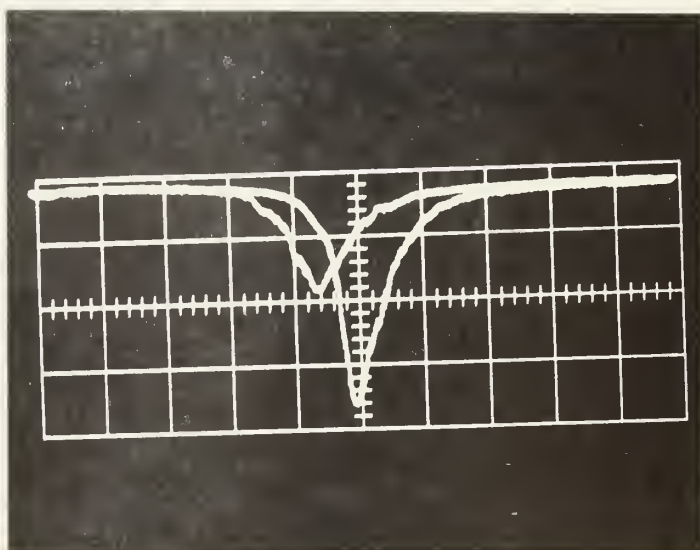
FABRY-PEROT
PERTURBATION OUTPUT

$H_2 = .48 \text{ CU.FT./HR.}$
 $O_2 = .2 \text{ CU.FT./HR.}$

FIGURE 25B

FABRY-PEROT
PERTURBATION OUTPUT

$H_2 = .6 \text{ CU.FT./HR.}$
 $O_2 = .15 \text{ CU.FT./HR.}$



a heated condition. The lineshift change due to water can be estimated relative to pure nitrogen from Eq. 2.32 for perpendicular incident light ($\theta = 0$). From Eq. 2.32

$$\Delta q = \frac{2L}{\lambda} \Delta n \quad 4.1$$

The change in the index of refraction due to the presence of water and nitrogen compared to that of only nitrogen must be found. The index of refraction of the mixture of nitrogen plus water can be written

$$n_1 = P_{H_2O} n_{H_2O} + (1 - P_{H_2O}) n_{N_2} \quad 4.2$$

where n_{H_2O} and n_{N_2} are the indices of refraction of water vapor and nitrogen, P_{H_2O} is the partial pressure of water. If complete conversion is assumed the partial pressure of water, assuming a .48 cu.ft./hr. flow rate of H_2 and 8 cu.ft./hr. flow rate of N_2 , is

$$P_{H_2O} = \frac{.48}{8.48} = .057 \text{ atm.} = \frac{43}{760} \quad 4.3$$

With $\Delta n = n_{N_2} - n_1$ Eq. 4.1 becomes

$$\Delta q = \frac{2\ell}{\lambda} P_{H_2O} (n_{N_2} - n_{H_2O}) \quad 4.4$$

For $P_{H_2O} = \frac{43}{760}$, $\eta_{N_2} = 1.000298$ and $\eta_{H_2O} = 1.000250$

Eq. 4.4 becomes

$$\Delta q = .102$$

or .102 of an order. For a finesse of 30 this is 3.1 linewidths. This variation is enough to cause the change in Fig. 25a,b. One point must be made, the values for η_{H_2O} and η_{N_2} were taken as those measured at approximately 6500 Å because these were the only readily available quantities. The actual values at 10.6μ may be different from those above resulting in a different linewidth change.

As an example from Fig. 25 and the theory developed the susceptibilities can be determined. From a flow rate of H_2 of .48 cu.ft./hr. Eq. 3.1 gives a filling factor of $f = 3.4 \times 10^{-5}$. From Eq. 2.44 and a finesse of 31 the total distance Z traveled by the beam is 197 cm. Now using Eq. 2.39 with $S = .69$, $\chi'_e = .25$. From Eq. 2.17 $\sigma_c/V = 1.38 \times 10^2$ and finally from Eq. 2.15 and 2.16 $\chi''_e = 6.98 \times 10^{-2}$ for 10.6μ radiation.

Figure 26 is an example of the resonance response for a cavity finesse of 31 and H_2 and O_2 flow rates of .31 cu.ft./hr. and .13 cu.ft./hr. respectively. Figure 27 represents the resonance response for $H_2 = .48$ cu.ft./hr. and $O_2 = .15$ cu.ft./hr. and the same cavity finesse. Figure 28 is the same response with flow rates of $H_2 = .24$ cu.ft./hr. and $O_2 = .15$ cu.ft./hr.

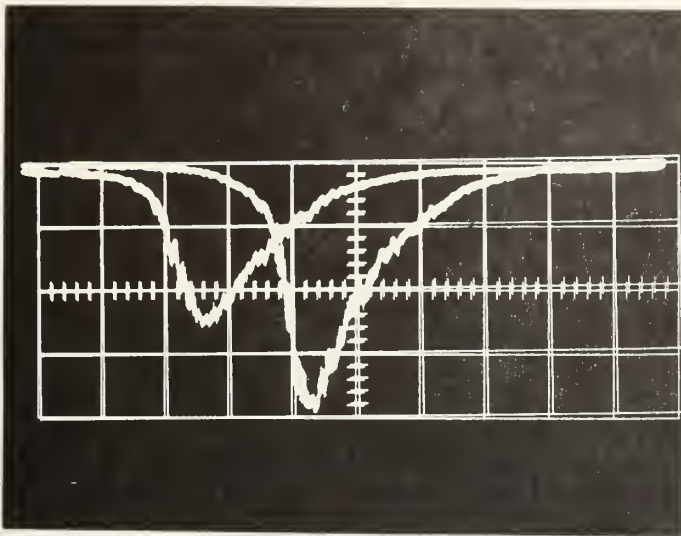


FIGURE 26

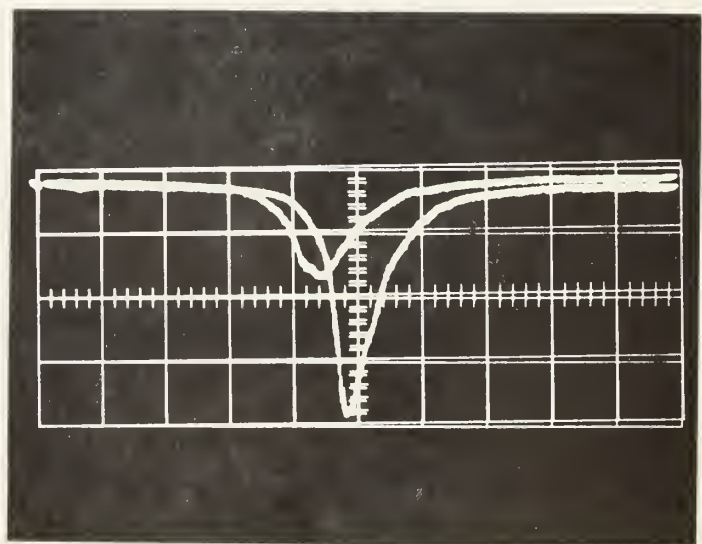
FABRY-PEROT
PERTURBATION OUTPUT

$H_2 = .31$ CU.FT./HR.
 $O_2 = .13$ CU.FT./HR.

FIGURE 27

FABRY-PEROT
PERTURBATION OUTPUT

$H_2 = .48$ CU.FT./HR.
 $O_2 = .15$ CU.FT./HR.



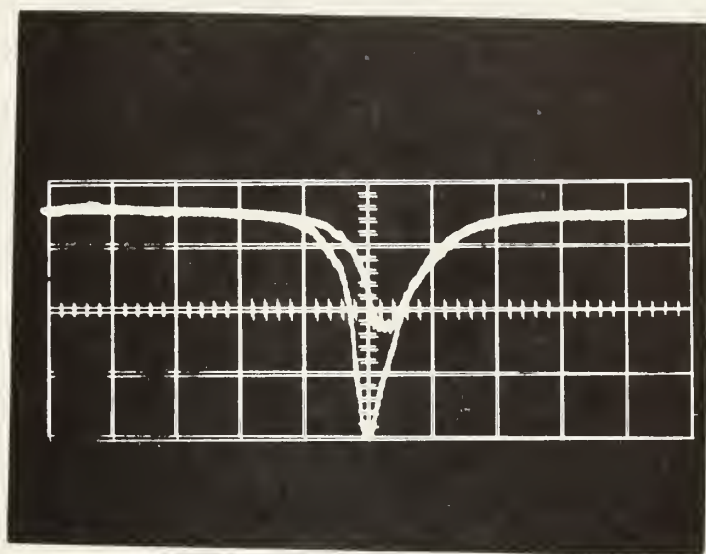


FIGURE 28

FABRY-PEROT PERTURBATION OUTPUT

$$H_2 = .24 \text{ CU.FT./HR.}$$

$$O_2 = .15 \text{ CU.FT./HR.}$$

In addition alignment of the particles by an external field was attempted. A 2 Hz, 500 v. potential was applied to two plates placed above and below the interferometer mirrors as previously described. No effect on the resonant peak due to this potential was observed.

The examples shown herein are illustrations of the measurements which may be achieved with the apparatus. They show excellent potential for the use of this system in future dielectric measurements. It can be expanded to measure relaxation frequencies and give information on particle size distributions. Also it is conceivable that if the system is calibrated for a particular substance, measurements of attenuation can give filling factor values. This makes the method useful to environmental pollution studies.

Certain inherent limitations are attributable to this system. One being that care must be taken to insure that the obtained results are due to the particles being studied and not to by-products of the reaction. Also the system requires disassembly and cleaning approximately every 2-3 days. One other stringent limitation of the Fabry-Perot interferometer is that it is expensive and applicable to only one wavelength, the mirror reflectivity being designed for one particular wavelength.

V. SUMMARY AND CONCLUSIONS

Starting with Maxwell's equations and the basic equations for a Fabry-Perot interferometer a method was developed to measure dielectric properties of suspensions of non-spherical particles in a gas. This was accomplished in two phases; 1) the multipass reflective cell which leads to a determination of the imaginary part of the extrinsic susceptibility and 2) the Fabry-Perot interferometer which can give both the real and imaginary parts of the extrinsic susceptibility. Also shown was how to relate this measured extrinsic susceptibility to the intrinsic susceptibility of the particle for spherical and rod geometries.

Utilizing the concepts developed, an experimental apparatus was developed to include the above cells and supporting equipment necessary to record the beam attenuation and phase change due to the introduction of a particulate suspension. Different cells were designed to find the ones which produced results in reasonable times and insured that the mirrors were protected from the suspension, the final method of mirror protection being an air curtain. A thermopile detector was used to detect the radiation in the multipass cell while a PbSnTe detector was used in the Fabry-Perot apparatus.

One reason for the development of both systems is that should only the attenuation be desired the multipass cell presents a quick and inexpensive method of measurement which is immediately applicable to a wide variety of wavelengths. Also since the total distance of the beam through the suspension is controllable, this method represents a more accurate method of measurement of the attenuation cross section. If both phase and attenuation are necessary the Fabry-Perot system must be utilized. Here because of the necessary high mirror tolerances the system is much more costly and must be designed for the wavelength region used. The Fabry-Perot interferometer is also susceptible to acoustic vibrations but these can be minimized through the use of a vibration isolation table. Both systems can readily be applied to a number of different aerosols.

Through the use of ZnO, Section IV shows the feasibility of this method of measurement. Initial cavity finesses on the order of 100 were easily available. Although the finesse degraded through use it still remained high enough to enable data to be taken. Since the multipass cell measured relative beam intensities the mirrors could be used for even greater periods of time, on the order of days, before disassembly and cleaning was necessary. Once cleaned the results returned to their initial values.

BIBLIOGRAPHY

1. Hedy, G. M., and Brock, J. R., Topics in Current Aerosol Research, Peragon Press, 1971.
2. Tolles, W. M., Sanders, R., and Fritz, G. W., "Dielectric Response of Anisotropic Polarized Particles Observed with Microwaves; A New Method for Characterizing the Properties of Non-Spherical Particles in Suspension," Journal of Applied Physics, Vol. 45, No. 9, September, 1974.
3. Debye, P., Polar Molecules, Chemical Catalog, 1929.
4. Frohlich, H., Theory of Dielectrics, 2nd ed., Oxford Press, 1958.
5. Dielectric and Related Molecular Processes, Vol. 1, The Chemical Society, Burlington House, 1972.
6. Stoner, E. G., "Demagnetizing Factors for Ellipsoids," Phil. Mag., Ser. 7, Vol. 36, No. 263, December 1945.
7. Born, M., and Wolf, E., Principles of Optics, Pergamon Press, 1970.
8. Lind, A. C., and Greenberg, J. M., "Electromagnetic Scattering by Obliquely Oriented Cylinders," Journal of Applied Physics, Vol. 37, No. 8, July 1966.
9. Hercher, M., "Spherical Mirror Fabry-Perot Interferometer," Applied Optics, Vol. 7, No. 5, May 1968.
10. Fork, R. L., Herriott, A. R., and Kogelnik, H., "A Scanning Spherical Mirror Interferometer for Spectral Analysis of Laser Radiation," Applied Optics, Vol. 3, No. 12, December, 1964.
11. Yariv, A., Introduction to Optical Electronics, Holt, Rinehart, and Winston, Inc., 1971.
12. Lax, B., and Button, K. J., Microwave Ferrites and Ferrimagnetics, McGraw-Hill Book Co., Inc., 1962.
13. Fritz, G. W., "Microwave Dielectric Response of Non-Spherical Particles by Modulation Techniques," Naval Postgraduate Thesis, March, 1974.
14. Myers, G. E., "Operating Lasers: Don't Be Half-Safe," Electro-Optical Systems Design, July, 1973.

15. Herriott, D., Kogelnik, H., and Kompfner, R., "Off-Axis Paths in Spherical Mirror Interferometers," Applied Optics, Vol. 3, No. 4, April, 1964.
16. Herriott, D. R., "Spherical-Mirror Oscillating Interferometer," Applied Optics, Vol. 2, No. 8, August, 1963.
17. Faxvog, F. R., "Detection of Airborne Particles Using Optical Extinction Measurements," Applied Optics, Vol. 13, No. 8, August, 1974.
18. Boyd, G. D., and Kogelnik, H., "Generalized Confocal Resonator Theory," Bell System Technical Journal, July, 1962, pp. 1347-1369.
19. Hill, N. E., Vaughan, W. E., Price, A. H., and Davies, M., Dielectric Properties and Molecular Behavior, Van Nostrand Reinhold Co., 1969.
20. Smyth, C. P., Dielectric Behavior and Structures, McGraw-Hill Book Co., Inc., 1955.

INITIAL DISTRIBUTION LIST

	No. Copies
1. Defense Documentation Center Cameron Station Alexandria, Virginia 22314	2
2. Library, Code 0212 Naval Postgraduate School Monterey, California 93940	2
3. Professor W.M. Tolles, Code 61T1 Department of Physics and Chemistry Naval Postgraduate School Monterey, California 93940	2
4. Professor G. E. Schacher, Code 61 Sq Department of Physics and Chemistry Naval Postgraduate School Monterey, California 93940	1
5. Capt. Anthony Raniszewski USMC 370 Kennedy Blvd. Bayonne, New Jersey 07002	1
6. Department of Physics and Chemistry Library Code 61 Naval Postgraduate School Monterey, California 93940	1
7. Dr. Tomas Leese, Code 40201 Naval Weapons Center China Lake, California 93555	1
8. Dr. William S. McEwan, Code 604 Naval Weapons Center China Lake, California 93555	1

Thesis
R213
c.1

161152

Raniszewski

A proposed method to
measure dielectric
properties of non-
spherical particles
using a Fabry-Perot
interferometer and
multipass reflective
cell.

Thesis
R213
c.1

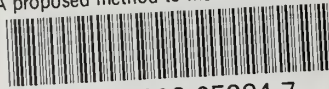
161152

Raniszewski

A proposed method to
measure dielectric
properties of non-
spherical particles
using a Fabry-Perot
interferometer and
multipass reflective
cell.

thesR213

A proposed method to measure dielectric



3 2768 002 05284 7
DUDLEY KNOX LIBRARY